Direct ink writing of vancomycin loaded polycaprolactone/ polyethylene oxide/ hydroxyapatite 3D scaffolds

Bin Zhang[a], Alexander K. Nguyen[b], Roger J. Narayan[b†], Jie Huang[a†]

[a] *Department of Mechanical Engineering, University College London, London, London, WC1E 6BT, UK*

[†]*Corresponding author. E-mail address: jie.huang@ucl.ac.uk*

[b] *Joint UNC/NCSU Department of Biomedical Engineering, North Carolina State University, Raleigh, NC 27695, USA*

[†]*Corresponding author. E-mail address: roger_narayan@unc.edu*

Abstract

Novel inks were formulated by dissolving polycaprolactone (PCL), a hydrophobic polymer, in organic solvent systems; polyethylene oxide (PEO) was incorporated to extend the range of hydrophilicity of the system. Hydroxyapatite (HAp) with a weight ratio of 55-85% was added to the polymer-based solution to mimic the material composition of natural bone tissue. The direct ink writing (DIW) technique was applied to extrude the formulated inks to fabricate the predesigned tissue scaffold structures; the influence of HAp concentration was investigated. The results indicate that in comparison to other inks containing HAp (55%, 75%, and 85%w/w), the ink containing 65% w/w HAp had faster ink recovery behavior; the fabricated scaffold had a rougher surface as well as better mechanical properties and wettability. It is noted that the 65% w/w HAp concentration is similar to the inorganic composition of natural bone tissue. The elastic modulus values of PCL/PEO/HAp scaffolds were in the range of 4 to 12 MPa; the values were dependent on the HAp concentration. Furthermore, vancomycin as a model drug was successfully encapsulated in the PCL/PEO/HAp composite scaffold for drug release applications. This paper presents novel drug-loaded PCL/PEO/HAp inks for 3D scaffold fabrication using the DIW printing technique for potential bone scaffold applications.

Keywords: direct ink writing; hydroxyapatite; ink rheology behavior; mechanical property; drug release; bone tissue scaffold.

1 Introduction

The repair of bone defects is an important focus area in orthopedic surgery; the current surgical treatments depending on the lesion size and severity include microfracture, autograft, allograft, and total joint replacement (1, 2). However, those treatments have drawbacks, including the quality inconsistency of the tissue obtained from microfracture (3), limitations in the autograft supply, immune rejection of allograft tissue (4, 5), as well as wear and loosening of prostheses (2). Bone tissue engineering therapies are attractive due to their potential to create biological substitutes that can maintain, replace, or regenerate bone tissue (1, 6).

Ideally, a bone scaffold should closely mimic the physiological properties of natural bone tissue; for example, a tissue scaffold should possess mechanical properties that match the host tissue as well as appropriate porosity and interconnectivity for nutrient delivery and tissue regeneration (7, 8). Particularly, bone scaffolds with pores larger than 300 μm facilitate the penetration of mineralized tissue and cell migration towards the scaffold center, stimulating nutrient supply and waste product removal (6, 9). In addition, the main chemical components of natural bone tissue are inorganic materials (e.g., calcium phosphate, 50-70% w/w) and organic materials (e.g., collagen, 30-50% w/w); the calcium phosphate mainly exists in the form of crystallized hydroxyapatite (HAp) and bonds with microfibril collagen. Thus, to mimic the chemical composition of natural bone tissue, an appropriate material for bone scaffold fabrication is a bioceramic-polymer composite that consists of both organic and inorganic components.

Over the past decades, extensive efforts have been made towards creating porous bone tissue scaffolds, from the traditional fabrication methods (e.g., freeze-casting, gas-foaming) that result in heterogeneously porous foams, to the 3D printing technologies that can be used to create ordered porosity and user-defined constructs. 3D printing techniques have been used to fabricate porous bone tissue scaffolds such as powder-based printing, liquid-based printing (e.g., DIW printing), and solid-based printing (e.g., fused deposition modeling). In comparison with other types of 3D printing techniques, the DIW method has the advantage of operating without the addition of heat, enabling the platform to accommodate inks containing thermolabile components (10). DIW printing involves the extrusion of pre-formulated inks through a nozzle with a displacement driving system; the inks can be in the form of a slurry or solution depending on the comprising polymers, solvents, and additives (11). The inks should meet specific rheological requirements for the scaffold fabrication with DIW printing: (1) the inks should form cohesive filaments after extrusion, (2) the inks should possess shear-thinning properties, and (3) the ink viscosity recovery behavior should be greater than 80% after extrusion (12-15).

Polycaprolactone (PCL) is a synthetic biodegradable polymer that has been widely used as a major component of bone tissue scaffolds (16, 17). PCL is known for its ease of forming of blends and composites, which can be used to modulate physical properties to enhance and expand its usability. Remya et al. (18) blended hydrophobic PCL with poly(ethylene oxide) (PEO), a hydrophilic polymer, to fabricate PCL/PEO hybrid fibers using electrospinning. The in vitro results show that the PCL/PEO sample degraded faster in phosphate buffer saline than PCL alone; in addition, there was enhanced cell attachment and proliferation on the PCL/PEO

samples as a result of improved surface wettability. HAp is a bioactive ceramic that is similar to the inorganic material in natural bone (19, 20). It has been demonstrated to possess osteoconductive properties (21). The combination of PCL/HAp and PCL/PEO/HAp based materials has previously been investigated for tissue scaffold fabrication (22, 23). Those studies demonstrate that a PCL-based polymer and HAp can mimic the organic and inorganic phases of natural bone tissue, respectively. For example, Kim et al. (23) developed a PCL/HAp composite bone tissue scaffold using the direct ink writing method. Their results indicate that the scaffold elastic modulus increased from 5.57 to 6.73 MPa when the HAp content rose from 0 to 20% w/w. Cui et al. used injection molding to develop a PCL/PEO/HAp composite scaffold. Their results show that the addition of HAp significantly improved the mechanical properties of the composite scaffolds (22). However, to the best of the authors' knowledge, the combination of PCL/PEO/HAp has not been investigated via DIW printing to date; furthermore, there is no systematic investigation of the ink optimisation progress. Thus, PCL/PEO/HAp based composite ink system is of interest in this study.

Vancomycin (VAN) is a glycopeptide antibiotic usually utilized against Gram-positive bacteria, including Staphylococcus aureus bacteria that are responsible for infection of the bone tissue (osteomyelitis). Considering its ototoxicity and nephrotoxicity via intravenous administration, the localized and controlled deployment of vancomycin offers a unique opportunity to deliver this antibiotic (24, 25). Previous studies have shown that bone tissue scaffolds containing VAN accelerated bone repair (25, 26). Meanwhile, VAN is a relatively thermal-sensitive drug and starts degrading at 42^{o}C (27). Compared with other 3D printing techniques, direct ink writing 3D printing of scaffold with VAN would be a wise option as its heat-free fabrication process. In this paper, PCL/PEO/HAp composite inks with various HAp concentrations were used to prepare for 3D scaffold fabrication via DIW printing. VAN was incorporated within the inks to fabricate composite scaffolds and the drug release properties of the composites were investigated. The aims of this study are to (1) study the rheology of processible PCL/PEO/HAp inks, (2) investigate the influence of HAp concentration on the surface properties and mechanical properties of the DIW printed 3D scaffolds, and (3) evaluate the drug release properties of the composite scaffolds.

2 Materials and methods

2.1 Materials

Polycaprolactone (PCL; average Mn ~ 80,000) and polyethylene oxide (PEO; average Mn ~ 200,000) were purchased from Sigma-Aldrich (St. Louis, MO, USA). Dichloromethane (DCM), 2-butoxyethanol (2-Bu), and dibutyl phthalate (DBP) were obtained from VWR International Ltd (Radnor, PA, USA). Hydroxyapatite (HAp) nanoparticles with a particle size less than 40 nm were purchased from SkySpring Nanomaterials, Inc. (Houston, TX, USA). All of the chemicals were used as received without further purification.

2.2 Ink formulation

2.2.1 Formulation procedure

Inks were formulated by dissolving 5-15% w/w polymer (i.e., PCL and PEO) in DCM, 2Bu, and DBP (2:1:1) by magnetic stirring at 200 rpm for 2 hours at 35ºC. After the PCL fully dissolved in the DCM/2Bu/DBP mixed solvent, PEO was added to the PCL solutions with a weight ratio of 0.5-2 followed by an additional 3 hours of stirring. Inks were prepared with the aid of a manual dispensing assessment based on the study by Zhang et al. (28). Considering the formulated inks cannot be either too liquid or too viscous for the filament formation, a weight ratio of PCL/PEO as 1:1 was finally chosen for the experiments. HAp nanoparticles were gradually added to the PCL/PEO solution to create HAp to polymer weight ratios of 55%, 65%, 75%, and 85%; the corresponding HAp volume fractions were 30.2%, 39.5%, 51.3%, and 66.3%, respectively. The resulting material was stirred for 8 h at 35ºC to obtain the homogenous solution. Those formulated inks with HAp concentrations of 55%, 65%, 75%, and 85% w/w were named as *PCL/PEO/55%HAp*, *PCL/PEO/65%HAp*, *PCL/PEO/75%HAp*, and *PCL/PEO/85%HAp*, respectively.

2.2.2 Ink characterization

20-gauge (G) nozzle tip with 20 mm in length was attached to the 3 mL syringe (Supplementary Figure 1 (a)). During the manual dispensing test, inks were consistently extruded under the manual pressure on the plunger and the process was recorded by the camera (Canon EOS M50, Canon, Melville, LA, USA).

The rheological measurements of the formulated inks were measured at 21ºC using a Discovery Hybrid Rheometer (DHR-3, TA Instruments, New Castle, DE, USA) with a 25 mm plate-plate (0.5 mm distance) and a solvent trap to prevent solvent evaporation during the measurements. 0.5 mL inks were extruded on the plate, and five replicates were taken for each measurement. To reduce the influence of solvent evaporation on the rheological testing results, continuous flow ramps were performed by varying the shear rate logarithmically from 0.5 to 50 s^{-1}. To simulate the 3D printing conditions, a creep recovery test was carried out to characterize the ink recovery behavior using three intervals; this process involved applying a shear rate of 0.1 s^{-1} for 70 s, followed by a high shear rate of 50 s^{-1} for 130 s, followed by a recovery interval with a shear rate of 0.1 s^{-1} for 100 s. The viscosity recovery percentage is defined by Equation 1:

$$\text{Viscosity recovery percentage} = \frac{\eta_{\text{recovery}}}{\eta_{\text{intial}}} \quad \text{Equation 1}$$

where $\eta_{recovery}$ is the viscosity at a recovery time at 300 s and $\eta_{initial}$ is the initial viscosity at 70 s.

2.3 3D scaffold fabrication

2.3.1 Structure design

Computer-aided design (CAD) software SolidWorks (Dassault Systèmes, Waltham, MA, USA) was applied to design a fifteen-layer woodpile 3D construct (Supplementary Figure 1 (b)). The length (D_1), width (D_2), and thickness (H_1) of the 3D construct are

14 mm, 14mm, and 5 mm, respectively. Each layer is comprised of parallel filaments with a width of 603 µm, which is equivalent to the diameter of a 20 G nozzle. The subsequent layers were stacked at 90º in the transverse plane to the prior level. G-codes were written using MATLAB software (MathWorks, Natick, MA, USA) in accordance with the designs of the CAD models, which gave instructions to the DIW printer to control the printing parameters as well as the position of the work stage and nozzles in the *X*, *Y*, and *Z* direction.

2.3.2 Mathematical model

The DIW operation parameters (Supplementary Figure 1 (c)), such as the printing speed on the *XY* plane (V_{XY}) and ink velocity on *Z*-axis (V_Z) and the extruded fluid rate (Q_E), were investigated based on the study by Zhang *et al.* (28). The velocity profile along a nozzle tube on the *Z* direction is given by Equation 2 according to the power law fluid model (29):

$$V_Z = \left(\frac{d}{2}\right)^{1+\frac{1}{n}} \left(\frac{\Delta P}{2mh}\right)^{\frac{1}{n}} \left(\frac{n}{n+1}\right) \left[1 - \left(\frac{2r}{d}\right)^{1+\frac{1}{n}}\right] \quad \text{Equation 2}$$

where ΔP is the pressure difference between the inlet and outlet of a printing nozzle. *r* is the radial coordinate, and *d* and *h* are the nozzle diameter and needle length, respectively. The extrusion flow rate Q_E and the generated wall shear rate $\dot{\gamma}$ are defined by Equation 3 (29) and Equation 4 (30).

$$Q_E = \left(\frac{\Delta P d}{4mh}\right)^{\frac{1}{n}} \left[\frac{n\pi d^3}{8(3n+1)}\right] \quad \text{Equation 3}$$

$$\frac{d_{V_z}}{d_r}|_{\frac{2}{d}} = \dot{\gamma} = \frac{32Q_E}{\pi d^3}\left(\frac{3}{4} + \frac{1}{4n}\right) \quad \text{Equation 4}$$

The nozzle diameter influences the shear rate. When the nozzle diameter *d* is fixed, the wall shear rate ($\dot{\gamma}$) increases with the extrusion flow rate. When the extrusion flow rate (Q_E) is fixed, the smaller nozzle diameter requires a higher pressure to extrude the ink. In this study, the extrusion flow rate was set to mimic the DIW printing process, the relationship between the HAp concentration and the DIW printing parameters was studied.

The relationship between the displacement (*E*) of the piston during the printing process, the extrusion flow rate Q_E, and printing speed V_{XY} is defined by Equation 5.

$$E = \frac{4Q_E L}{V_{XY}\pi D^2} \quad \text{Equation 5}$$

where D is the inner diameter of the syringe that is applied to extrude the ink, and L is the printed filament length. The value of E was set within the G-code for DIW printing; it is dependent on the presetted extrusion rate Q_E, and printing speed V_{XY}.

2.3.3 DIW printing process

A R3bel 3D bioprinter (SE3D, Santa Clara, CA, United States), a piston extrusion-based printer, was used to fabricate the scaffolds (Supplementary Figure 1(c)). There are three subsystems in the DIW fabrication system, which are the data processing system, the material preparation system, and the DIW printing system. In data processing system, the G-codes of the designs were generated using MATLAB in accordance with the predesigned CAD models. The G-code was developed to control the relative positions of the work stage and the nozzle to carry out the ink extrusion process and form the 3D scaffold in a layer-by-layer manner.

The continuity and consistency of the PCL/PEO/HAp composite inks extrusion process are of great importance during the DIW printing process. The extrusion process can be affected by the ink rheology behavior and the processing parameters (i.e., the printing speed and extrusion rate). To optimize the DIW printing parameters, a flow rate of 0.8-2.4 mm^3/s and printing speed in the range from 2.5 to 12.5 mm/s were set using Pronterface software (https://pronterface.com). The motion system is comprised of the work stage and nozzle. The work stage moves in horizontal directions while the nozzle moves in both horizontal and vertical directions. A 3 mL syringe is used to carry out the extrusion. A glass slide was put on the workbench before extrusion, which provided a smooth and flat surface; the scaffolds were removed from glass slides after fully drying.

2.4 3D scaffolds characterization

2.4.1 Physicochemical characterization

Fourier transform infrared (FTIR) analysis was used to characterize the chemical structure of pure HAp, PCL, and PEO, as well as the DIW printed PCL/PEO/HAp and the VAN loaded PCL/PEO/HAp composite scaffold. FTIR absorbance spectra of the samples were collected using a Perkin Elmer 2000 FTIR spectrophotometer (PerkinElmer, Inc., Waltham, Massachusetts, USA). The spectra were collected over a wavenumber range of 500-4000 cm^{-1}.

The crystal structure and phases of the DIW printed scaffolds were investigated via powder X-ray diffraction (pXRD) using a D5005 diffractometer (Siemens, Munich, Germany) with monochromatic CuKα radiation (wavelength =1.54056 Å). The samples were scanned from a 2θ angle of 15° to 60° at a step size of 0.02º and a scan rate of 0.02º/min. Each sample was analyzed in triplicate, and the average was compared.

2.4.2 DIW printed pattern and surface morphology

The surface morphology of the printed samples was evaluated using scanning electron microscopy (SEM) with a Model S-3200N instrument (Hitachi, Tokyo, Japan). The samples were first sputter-coated with gold (10 nm); the images were taken at magnifications from ×500 to 10k with an acceleration voltage of 5 kV. The DIW printed filament width was quantified using a statistical distribution that involved measurement of 50 filaments in Image J software; the data was exported for analysis, and graphs were plotted using Origin software (OriginLab, Northampton, MA, USA). Error bars were plotted to represent the mean ± standard error. The index of relative filament deviation ($\sigma_{filament}$) was proposed to evaluate the printing fidelity, which was defined in Equation 6.

$$\sigma_{filament} = \frac{W_{filament}}{d} - 1 \qquad \text{Equation 6}$$

where *d* is the applied nozzle diameter as indicated earlier and $W_{filament}$ is the DIW printed filament width. By varying the printing parameters (i.e., the extrusion flow rate (Q_E) and printing speed (V_{XY})), the index of relative printing deviation ($\sigma_{filament}$) was altered.

The surface roughness of the samples was quantified using a VKx1100 confocal laser scanning microscope (Keyence, Osaka, Japan). The roughness was measured over an area of 600 μm (length) × 60 μm (width) for three different filaments on the sample surface. The surface roughness in terms of an arithmetic average (Ra) was obtained as a function of the printing conditions.

2.4.3 Micro-CT scan analysis

A ZEISS X radia 510 Versa X-ray microscope (Carl Zeiss AG, Jena, Germany) was used to image 3D printed scaffold samples. Projection images were taken at 25 kV and 193 mA, with 0.434° rotation steps, a 2 s image acquisition time, and a pixel size of 5 μm. The resulting binary 3D dataset was reconstructed using Simpleware software (Synopsys, Mountain View, California, United States). The horizontal filament distance/pore size and vertical filament distance of the reconstructed 3D constructs were measured. Detailed information about the horizontal and vertical filament distance is shown in Figure 7 (a). The porosity of 3D constructs was calculated based on Equation 7:

$$Porosity = 1 - \frac{V_{solid}}{V_{total}} \qquad \text{Equation 7}$$

where V_{total} (scaffold length *width * height), scaffold length, width, height, and V_{solid} were directly measured in Simpleware software.

2.4.4 Surface wettability

Contact angle measurements were performed to evaluate the surface wettability of the DIW printed scaffold. The contact angle was measured with the sessile drop method by depositing ultrapure water ($4x10^{-3}$ μL) on the filament surfaces of the DIW printed scaffolds using an optical contact angle meter (OCA 15EC; Dataphysics Instruments GmbH, Filderstadt, Germany). All of the measurements were performed at 21°C, and the gradual change of water contact angle was captured with a digital camera at three different places on each sample.

2.4.5 Mechanical properties

The stress-strain relationships of the DIW printed PCL/PEO/HAp scaffold specimens were tested in uniaxial compression experiments using a UniVert universal testing machine (CellScale, Waterloo, Canada). Scaffolds with various HAp concentrations (55-85% w/w) were tested; each type of scaffold was measured using four replicates. In the compression tests, a preload of 1 N was applied to each sample, followed by a compression of 1 mm/minute. The test was stopped when the maximum force capacity of the load cell was reached. The yield point, which represents the transition from elastic to plastic deformation, was recorded. Elastic modulus values of the scaffold samples were calculated from the linear region according to ASTM: D695-02a (2002), the standard test method for compressive properties of rigid plastics (31, 32). To analyze the results, the width and length of DIW printed samples were measured with vernier caliper; the area of the sample was calculated by multiplication of sample width and length. The strain was calculated from the displacement divided by the thickness of the printed samples. The scaffold thickness was detected by the testing machine during the compressive test. The elastic modulus was taken as the slope of the linear region of the stress-strain curve before the yield point.

2.5 Scaffolds loaded with drug

2.5.1 Drug incorporation

The inks with drug loading were prepared by gradually adding vancomycin (VAN) into the *PCL/PEO/65%HAp* ink with concentrations of 3 or 9% w/w and stirring for 4 h at 35ºC to obtain a homogenous solution. The PCL/PEO/HAp composite and drug concentrations are listed in Table 1. The inks with VAN concentrations of 3% and 9% w/w were named *PCL/PEO/HAp_3%VAN* and *PCL/PEO/HAp_9%VAN*, respectively. The DIW printing process parameters for drug-loaded ink were the same for printing the *PCL/PEO/65%HAp* ink.

2.5.2 In vitro dissolution test

An in vitro dissolution test was conducted in a shaking incubator using a KS 3000 i control incubator shaker (IKA, Königswinter, Germany) for eight hours. DIW printed composite scaffolds loaded with VAN were weighed before dropping into the preheated

glass tubes, which contained 100 mL of PBS (pH 7.4). A constant temperature of 37°C and a rotational speed of 100 rpm were used throughout the experiments. Samples of 3 mL were taken at time points of 15 min, 30 min, 1 h, 2 h, and 4 h; each time the same volume of release medium was replaced. The absorbance of the collected samples was measured using UV/VIS spectrophotometry (VWR, Leuven, Belgium) at λ = 280 nm, the maximum absorption wavelength of VAN. The drug content was calculated according to the developed calibration curve. Each experiment was conducted in triplicate.

2.5.3 Statistical analysis

All quantitative data were expressed as the mean ± standard error. Numerical data were analyzed via Student's t-test to determine the differences among the groups. Statistical significance is indicated if p-values ≤ 0.05 represents as (*) while no significance if p-value > 0.05.

3 Results

3.1 Ink printability assessment

Manual dispensing is the first assessment step, which can rapidly and effectively determine whether the ink can form as a cylindrical filament. A 20 G stainless steel nozzle was used for the manual dispensing testing, which corresponds to an inner nozzle diameter of 603 µm. The dispensing behavior of inks with HAp concentrations from 55 to 85% w/w was evaluated (Supplementary Figure 1 (a)). The inks *PCL/PEO/55%HAp*, *PCL/PEO/65%HAp*, *PCL/PEO/75%HAp*, and *PCL/PEO/85%HAp* were able to form as filament shapes. The results imply that these inks could meet the first assessment requirement for DIW printing.

The second assessment step involves rheological measurements. Routine rheology measurements were performed to characterize the shear rate-dependent viscosity and recovery behavior of the formulated inks. The viscosity of the PCL/PEO/HAp inks with HAp concentrations from 55 to 85% w/w were evaluated through steady-state shear viscosity measurements as shown in Figure 1 (a). By applying the power-law model to fit the shear rate-viscosity profiles, the degree of shear-thinning was determined by calculating the consistency index and power-law index (29), which is given by Equation 8.

$$\eta(\dot{\gamma}) = m\dot{\gamma}^{n-1} \qquad \text{Equation 8}$$

In this equation, *m* is the consistency index and *n* is the power law index. The value of *m* is associated with the magnitude of the viscosity, and the value of *n* defines the viscosity behavior: (i) shear-thinning if $n < 1$, (ii) shear-thickening if $n > 1$, or (iii) Newtonian if $n = 1$. The curve of ln η -ln γ was obtained based on the ink viscosity curves. The consistency index *m* and power law index *n* for the PCL/PEO/HAp inks were obtained by fitting the slope and intercept.

Figure 1 (b) summarises the n and m values of PCL/PEO/HAp inks; their correlation coefficients (r^2) were greater than 0.99. The n values for all of the inks were less than 1, indicating that all of the inks are non- Newtonian fluids with shear-thinning behavior. The larger the deviation of n from 1, the more non-Newtonian the behavior of the fluid (33). The power law index (n) significantly decreased ($p \leq 0.05$) with an increase in the HAp concentration from 55 to 85% w/w for the PCL/PEO/HAp inks; this result indicates a more prevalent shear-thinning behavior.

Then, the ink viscosity recovery behavior was examined using the creep recovery test. This test corresponded to the DIW printing process: (a) inks tend to become oriented in the flow direction when inks flow through the nozzle tip; (b) the viscosity decreases and stays constant in the load-interval; (c) the viscosity recovery occurs with time after removal of the high shear rate. Gaharwar et al. (34) indicated that the inks with an initial viscosity recovery higher than 80% could be used for 3D printing. The result of the ink viscosity recovery test is presented in Figure 1 (c). For inks of *PCL/PEO/55%HAp*, *PCL/PEO/65%HAp*, *PCL/PEO/75%HAp*, and *PCL/PEO/85%HAp*, the recovery percentages were calculated using Equation 1 as 88%, 95%, 94%, and 74%, respectively, at 300 s. These results indicate that all of the formulated inks could meet the second requirement for DIW printability: low viscosity values at high shear rates and high viscosity values at the low shear rate. However, considering that the ink recovery percentage should be high enough (at least 80%) to maintain ink continuity and consistency during DIW printing, the *PCL/PEO/55%HAp*, *PCL/PEO/65%HAp*, and *PCL/PEO/75%HAp* inks are more suitable for DIW printing.

3.2 Mathematical analysis of ink flow within a printing nozzle

The theoretical extrusion behavior of inks within a printing nozzle was analyzed using the mathematical model as described by Equations from 2 to 5. The spatial distributions of extrusion rate, printing velocity, and shear rate were predicted for PCL/PEO/HAp inks with HAp concentrations from 55 to 85% w/w. The profiles of velocity in the Z direction (V_Z) of inks along a radial axis of 301.5 µm nozzle were calculated using Equation 4 as shown in Figures 2 (a-d). When the fluid extrusion rate increased from 0.8 to 2.4 mm^3/s, the extrusion pressure (ΔP) and generated wall shear rate ($\dot{\gamma}$) within a printing nozzle were raised; the velocity profile along with the needle nozzle in the Z direction (V_Z) decreased towards the needle wall. In Figures 2 (a), the results indicate that the velocity profile of *PCL/PEO/55%HAp* ink gradually decreased from the middle of the printing needle to the needle wall. In Figure 2 (d), the velocity (V_Z) of PCL/PEO/85%HAp ink kept a constant level within the needle until r = 0.15 mm, decreased gradually (r > 0.15 mm), then reached 0 at the nozzle wall (r = 0.3 mm).

As shown in Figure 3 (a), the ink shear-thinning behavior under extrusion (Q_E) is associated with a decrease in the ink viscosity; as such, the ink would flow out. Figure 3 (b) shows that the shear rate of four inks experienced a linear increase as a function of the extrusion rate (Q_E). Under an extrusion rate of 0.8 mm^3/s, the predicted shear rates that *PCL/PEO/55%HAp*, *PCL/PEO/65%HAp*,

PCL/PEO/75%HAp, and *PCL/PEO/85%HAp* inks experienced were 42.2 s^{-1}, 46.2 s^{-1}, 50.9 s^{-1}, and 60.8 s^{-1}, respectively. The *PCL/PEO/85%HAp* ink exhibited approximately 1.4 times more shear rate than the *PCL/PEO/55%HAp* ink. Figure 1 (c) shows that after experiencing shear rate (50 s^{-1}), the ink recovery percentage of *PCL/PEO/55%HAp* ink and *PCL/PEO/85%HAp* ink were 88% and 74%, respectively. The results suggest that after printing at an extrusion rate of 0.8 mm^3/s, the ink recovery rate of the *PCL/PEO/85%HAp* ink would be lower than that of the *PCL/PEO/55%HAp* ink.

3.3 Shape fidelity analysis

3.3.1 Effect of operational parameters

The extrusion rate (Q_E) and printing speed in the XY plane (V_{XY}) directly influence the shape fidelity for filament deposition. As shown in Figure 4 (a) for *PCL/PEO/55%HAp* ink, the printed filament width was varied by changing the printing speed (V_{XY}) when the extrusion rate was 0.8 mm^3/s. The printed filament width was 620 ± 3 μm when the print speed was 2.5 mm/s; this value was wider than the nozzle diameter (d = 603 μm). When the printing speed was 5 mm/s, the printed filament width was similar to the nozzle diameter; the width of the deposited filament was 600 ± 8 μm. When the velocity increased to 12.5 mm/s, the printed filament width was 420 ± 7 μm, which was lower than the nozzle diameter.

Figure 4 (b, c, d, e) shows the DIW printed filament width of four types of PCL/PEO/HAp inks under various extrusion fluid rates (Q_E) from 0.8 to 2.4 mm^3/s as well as the printing speeds (V_{XY}) from 2.5 to 12.5 mm/s. The first layer of the 3D construct was printed to access the relationship between filament width and printing parameters (i.e. extrusion rate and printing speed). The DIW printed filament width increased with a decrease in print velocity (V_{XY}) or an increase in fluid extrusion rate (Q_E), and vice versa. Filament width measurement was not performed for filament widths exceeding interfilament distance; adjacent filaments would be fused together.

The relative filament deviation index ($\sigma_{filament}$) was used to evaluate the shape fidelity of the DIW printed filaments as calculated from Equation 6. The $\sigma_{filament}$ approached 0 when the filament width ($W_{filament}$) matched the nozzle diameter (d). The relative filament deviation indexes at various extrusion fluid rate (Q_E) and print velocity (V_{XY}) values were compared in Figure 5 (a, b, c, d). Optimization of the shape fidelity ($\sigma_{filament}$ was closest to 0) was demonstrated at a printing speed V_{XY} of 5 mm/s and a fluid extrusion rate Q_E of 0.8 mm^3/s for the inks *PCL/PEO/55%HAp* and *PCL/PEO/65%HAp*. Similarly, a printing speed (V_{XY}) of 7.5 mm/s and an extrusion fluid rate (Q_E) of 0.8 mm^3/s were optimal for the inks *PCL/PEO/75%HAp* and *PCL/PEO/85%HAp*. These operation parameters were subsequently used to build the 3D scaffolds in a layer-by-layer manner.

3.3.2 DIW printed 3D constructs

The printed 3D scaffolds *PCL/PEO/55%HAp, PCL/PEO/65%HAp, PCL/PEO/75%HAp* and *PCL/PEO/85%HAp* were built in a layer by layer manner. The images of the printed samples, showing 12 layers, are provided in Figure 6 (a). In Table 2, the printed dimensions (width, length, and thickness) of the scaffolds were smaller than the CAD theoretical values. Previous studies (35, 36) also show similar results and reflected the shrinkage issue of the DIW printed scaffolds. With the increase in HAp concentration, the difference between the theoretical values and experimental values in terms of width, length, and thickness gradually decreased. The filament width ($W_{filament}$) of the top layer of the DIW printed scaffolds were compared with the applied nozzle diameter (d) in Figure 6 (b). A comparison of the relative filament deviation indexes ($\sigma_{filament}$) from the top layers of all of the DIW printed samples is shown in Figure 6 (c). This result confirms that all of the samples have shrinkage due to relative filament deviation indexes ($\sigma_{filament}$) that were less than 0. The printed filament of *PCL/PEO/85%HAp* was most closely matched to the nozzle diameter (d); the σ_{filament} was the closest to 0. This is possibly due to adding nanoceramic particles into solvent-based polymeric matrix could help with the filament solidification, which is desirable for preventing sagging of the filaments when spanning features are manufactured, particularly in porous 3D constructs (37, 38).

It is noted that although the shape fidelity test was implemented for the first layer printing for all types of inks (described in section 3.3.1), filament deviation still existed due to shrinkage, which commonly happens to the direct ink writing 3D construct after drying. A few parameters (e.g., shrinkage ratio and sagging between intersection layers) could affect the top layer filament shape fidelity. The relative filament deviation mentioned in this study could optimize the 3D printing parameters to confirm that the filament diameter at the top layer after drying is as similar as the designed nozzle size.

3.3.3 Micro-CT scan analysis

Micro-CT imaging was used to investigate the horizontal filament distance/pore size (d_{xy}) and vertical filament distance (d_z), and porosity of DIW printed PCL/PEO/HAp scaffold as shown in below (Figure 7 (a)). Both the horizontal and vertical filament distance are important factors in terms of allowing vascularization and cell migration (39, 40). The theoretical horizontal and vertical filament distance of CAD model are 500 µm and 300 µm, respectively. The horizontal filament distances for DIW printed samples of *PCL/PEO/55%HAp, PCL/PEO/65%HAp, PCL/PEO/75%HAp, and PCL/PEO/85%HAp* were 0.59±0.01 mm, 0.58±0.02 mm, 0.52±0.02 mm and 0.50±0.02 mm, respectively. The vertical filament distances for DIW printed samples of *PCL/PEO/55%HAp, PCL/PEO/65%HAp, PCL/PEO/75%HAp, and PCL/PEO/85%HAp* were 0.15±0.02 mm, 0.22±0.03 mm, 0.25±0.03 mm and 0.30±0.01 mm, respectively. Horizontal filament distance (d_{XY}) gradually decreases while the vertical filament distance (d_Z) gradually increases when the HAp concentration increases from 55% to 85% w/w. This result corresponds to the filament width of 3D printed construct in Figure 6 (b).

Meanwhile, the theoretical porosity of CAD model is 49%. In Figure 7 (b), the porosity of the DIW printed PCL/PEO/HAp 3D construct increased from 38.8±2.7% to 53.1±1.1% ($p \leq 0.05$, significant difference) when the HAp concentration was raised from 55% to 85% w/w. This result may be attributed to filament solidification from the addition of nanoHAp particles into the solvent-based polymeric matrix; this phenomenon is desirable for preventing sagging of the filaments when spanning features are manufactured, particularly in porous 3D constructs (37, 38).

3.4 Mechanical properties

The compressive test was applied to evaluate the mechanical properties of DIW printed samples - *PCL/PEO/55%HAp, PCL/PEO/65%HAp, PCL/PEO/75%HAp, and PCL/PEO/85%HAp*. In Figure 8 (a), the compression experiment results indicate that the elastic modulus of PCL/PEO/HAp scaffolds significantly increased ($p \leq 0.05$) from 8.33 ± 0.98 MPa to 12.33 ± 0.29 MPa when the HAp concentration increased from 55% w/w to 65% w/w. However, elastic modulus values significantly decreased ($p \leq 0.05$) when the HAp concentration rose from 65% to 85% w/w; the elastic modulus values for *PCL/PEO/75%HA* and *PCL/PEO/85%HA* were 4.50 ± 0.57 MPa and 3.60 ± 0.29 MPa, respectively. The stress-strain curves of DIW printed samples are in Supplementary Figure 2. This result may be attributed to the complex interaction between the organic phase and HAp nanoparticles. Once HAp nanoparticle concentration increases above 65%w/w, the nanoparticles can behave like “defects” in the composite network (e.g., the HAp nanoparticles can aggregate and form larger particles), which contribute to failure of the material under mechanical loading. Figure 8 (b) contains SEM micrographs of the surface morphology of the DIW printed scaffolds, which show small cracks on top of the surface of the *PCL/PEO/75%HAp* and *PCL/PEO/85%HAp* scaffolds.

The yield strength values had the same trend as the elastic modulus values; yield strength values of 0.77 ± 0.03, 0.97 ± 0.03, 0.42 ± 0.02, 0.35 ± 0.05 MPa were obtained for the samples *PCL/PEO/55%HAp*, *PCL/PEO/65%HAp*, *PCL/PEO/75%HAp*, and *PCL/PEO/85%HAp*, respectively. This result indicates that the scaffold *PCL/PEO/65%HA* had significantly higher elastic modulus and yield strength compared to others ($p \leq 0.05$).

3.5 Surface morphology and wettability

The SEM micrographs showing the surface morphology of the DIW printed samples are provided in Figure 9 (a). The surface roughness of the DIW printed PCL/PEO/HAp was evaluated using surface roughness measurements, which are shown in Figure 9 (c). The sample roughness values (e.g., Ra, Rz, Rq) obtained from a quantitative analysis of the filament top layers are summarized in Table 3. The surface roughness (e.g., Ra, Rz, Rq) of *PCL/PEO/65%HAp* was significantly higher ($p \leq 0.05$) than that of *PCL/PEO/55%HAp*. Surface roughness also plays a role in cell adhesion, growth, and differentiation. The nanoscale roughness of the surface may support cell adhesion and growth. In addition, micro-roughness (100 nm-100 µm of Ra value) has been shown to improve osteogenic differentiation of the cells [22, 35]. It has previously been demonstrated that the proliferation of rat osteoblasts was improved with an increase of the surface roughness (in the range of 0–4 µm Ra) (41).

Contact angle (CA) is a measure of surface wettability, which indicates whether the material is hydrophilic (<90°) or hydrophobic (>90°) (42). The CA values from the top layer filament of DIW printed samples are shown in Figure 9 (b). A droplet volume of 4×10^{-3} μL was applied for the CA measurement; the droplet diameter was approximately 200 μm, which was smaller than the filament width (ranging from 420 to 570 μm). Thus, the CA approach was able to place the water droplets on top of a single filament. Figure 9 (c) shows the initial contact point of a droplet on the top layer filament of DIW printed samples. The initial CA results (drop age = 0 second) were 41.3 ± 7.6º, 15.1 ± 0.3º, 37.8 ± 6.4º and 23.8 ± 6.3º for *PCL/PEO/55%HAp*, *PCL/PEO/65%HAp*, *PCL/PEO/75%Hap*, and *PCL/PEO/85%HAp*, respectively. After 500 ms, the droplets absorbed into the filament of *PCL/PEO/65%HAp* samples, and the CA values (drop age = 500 ms) become 0, thus indicating that the filaments of *PCL/PEO/65%HAp* wetted entirely within less than 500 ms. For *PCL/PEO/55%HAp*, *PCL/PEO/75%HAp*, and *PCL/PEO/85%HAp*, the CA values at the drop age of 10 s were 32.5 ± 5.5º, 27.5 ± 3.7º, and 15.3 ± 5.1º, respectively. The *PCL/PEO/65%HA* scaffold showed the smallest CA values ($p \leq 0.05$).

3.6 Drug loaded 3D scaffolds

3.6.1 Material characterization

FTIR was used to understand the chemical bonding in the PCL, PEO, HAp, and PCL/PEO/HAp composite scaffolds (Figure 10a (a-d)). The FTIR spectra of the DIW printed VAN-loaded PCL/PEO/HAp scaffolds (Figure 10a (e, f)) and VAN (Figure 10a (g)) were also obtained. Characteristic absorption bands in PCL such as asymmetric CH_2 stretching vas (CH_2) at 2943 cm^{-1}, symmetric CH_2 stretching vs (CH_2) at 2865 cm^{-1}, and carbonyl stretching ν(C=O) appear at 1720 cm^{-1} were noted. The PEO spectrum showed a sharp band at 2865 cm^{-1}, which was assigned to C-H asymmetric stretching of the methylene group. The absorption band located at 1110 cm^{-1} corresponds to the C-O-C stretching mode. The HAp spectra show features associated with the phosphate group around 900 to 1300 cm^{-1} and the carbonate group between 850 and 890 cm^{-1}. VAN showed three peaks at 1506 cm^{-1}, which were attributed to the aromatic rings; features at 1588 cm^{-1} and 1652 cm^{-1} correspond to the amide I and amide II peaks, respectively. The intensity of the peaks at 1652 cm^{-1} was found to rise with an increase in the VAN concentration. This feature was not observed in PCL/PEO/HAp scaffolds that do not contain VAN. As shown in Figure 10a (f), features at 1506 cm^{-1} and 1588 cm^{-1} were detected only in scaffolds with a VAN concentration of 9% w/w.

The interaction between VAN and either PCL or PEO potentially occurs via hydrogen bond formation. The N-H moiety in the vancomycin molecule is capable of forming hydrogen bonds with the C-O-C moiety in PCL and PEO. The intensities of peaks at 1187 cm^{-1}, 1168 cm^{-1}, and 1095 cm^{-1}, attributed to OC-O stretching, symmetrical COC stretching, and C-O-C stretching vibration, were reduced. The reduced intensities of these peaks could indicate that OC-O and C-O stretching of PCL and PEO monomers were diminished, which may be caused by hydrogen bond formation between PCL and VAN. The FTIR spectra of drug-loaded scaffolds

showed no visible peak shifts compared with the unloaded scaffold (Figure 10). This result indicated that drug-composite interactions were weak after the DIW process. The PCL/PEO/HAp composite scaffold shows the main characteristic absorption bands of PCL, PEO, and HAp. The FTIR spectra also confirmed the presence of VAN in the DIW printed composite scaffold, suggesting that VAN was successfully encapsulated by DIW printing method to produce a drug/polymer/ceramic composite scaffold.

PXRD was used to determine the phase structure of the PCL/PEO/HAp composites. Figure 10b shows the pXRD pattern of the printed PCL/PEO/HAp scaffold. The peaks at angles 2θ = 21.4° and 23.8° correspond to the (110) and (200) crystallographic planes of the semi-crystalline nature of the PCL biopolymer (43). PEO exhibits two characteristic peaks at angles around 2θ = 23º, and 19º (44). HAp exhibits broad peaks, suggesting that the nanoparticle size is very small (45). The characteristic of peaks of PCL, PEO and HAp were unchanged in the PCL/PEO/HAp blends. Additionally, a broad feature was observed in the pXRD pattern of vancomycin from 2θ of 10° to 35°; this result indicates that VAN is amorphous (46). The pXRD patterns of the VAN loaded PCL/PEO/HAp samples - PCL/PEO/HAp_3%*VAN* and PCL/PEO/HAp_9%*VAN* were similar to that of PCL/PEO/HAp_without *VAN*. These results suggest that the crystallinity of the PCL/PEO/HAp was maintained after loading with VAN.

3.6.2 In vitro dissolution profile

The release kinetics of DIW printed PCL/PEO/HAp samples containing low and high VAN loading (3% and 9% w/w) were determined in vitro; the effect of drug loading on release profile was examined. The cumulative release profiles of VAN from the DIW printed constructs is shown in Figure 11. Total release values of 82.67 ± 0.06% and 91 ± 0.03% were obtained for *PCL/PEO/HAp_3%VAN* and *PCL/PEO/HAp_9%VAN*, respectively, after 480 min. The in vitro release profile results were in line with the literature data reporting an initial burst release of the incorporated drug followed by a slow-release phase (47, 48). Additionally, the release profiles revealed the formulation with a higher VAN loading released VAN faster than the formation with a lower drug loading, especially for the time points of 30 min, 60 min, and 120 min; the drug release results were 33.01%, 48.57%, 72.06% at 30 min, 60 min, and 120 min for *PCL/PEO/HAp_3%VAN* and 49.66%, 69.39%, 86.18% at 30 min, 60 min, and 120 min for *PCL/PEO/HAp_9%VAN*. SEM micrographs in Figure 11 (b, c, d) shows the surface morphology of *VAN*-free scaffold surface, VAN-loaded scaffold before and after the release study of sample *PCL/PEO/HAp_9%VAN*.

4 Discussion

An increase in the HAp concentration in PCL/PEO/HAp inks had a noteworthy impact on the ink rheological properties. The initial viscosity (when shear rate as 0.05 s^{-1}) of PCL/PEO/65%HAp inks was the highest, and the initial viscosity of the *PCL/PEO/85%HAp* inks was the lowest. This result may be due to the greater interchain bonding in the polymers within *PCL/PEO/65%HAp* inks than in the PCL/PEO/85%HAp inks, which in turn lead to higher viscosity values for the *PCL/PEO/65%HAp* inks at rest or low shear strains. This phenomenon also can be correlated with ink recovery behavior results. At the high shear rate (50 s^{-1}), the

PCL/PEO/65%HAp inks had the highest recovery percentage (95%); the *PCL/PEO/85%HAp* inks had the lowest recovery percentage (74%). Moreover, the power law index (n) of PCL/PEO/HAp inks decreased with the increase in the HAp concentration from 55% to 85% w/w. This result could be due to the difference in solute polarity between the polymer molecules and HAp particles. All inks showed the shear-thinning non-Newtonian behavior; however, an adequate recovery percentage of viscosity (>80%) with a time-dependent increase were only possible with the *PCL/PEO/55%HAp*, *PCL/PEO/65%HAp*, and *PCL/PEO/75%HAp* inks. This result implies that inks with a HAp concertation greater than 75% w/w (such as PCL/PEO/85%HAp ink) would not be an ideal printable material for DIW printing.

The mathematical analysis of ink flow within the nozzle was applied to predict the shear rate that the ink would experience during the extrusion process. This phenomenon is similar to a fully developed parabolic fluid profile within a pipe; internal friction in the fluid would resist flow motion (49, 50). When a fluid is in contact with a static solid surface (i.e., the needle wall), adhesion can reduce the fluid flow. The higher shear rate of the *PCL/PEO/85%HAp* ink and the lower recovery percentage after removal of a high shear rate (i.e., 50 s^{-1}) in the creep recovery test could make the *PCL/PEO/85%HAp* ink more prone to printing failure; the other inks may be more suitable for successful DIW printing via extrusion.

The elastic modulus and yield strength values are greater when HAp concentration increases from 55% to 65% w/w. Similar results also can be found in other studies (51, 52). However, when the HAp content increased up to 75% w/w, the elastic modulus and yield strength decreased. One possible reason could be related to the ink recovery behavior. The mechanical property results of the PCL/PEO/HAp scaffold were in line with the ink recovery percentage. Another possible reason is that small cracks were observed from the SEM images on the surface of DIW printed samples with more than 75% w/w HAp content. There was an increase of polymer and ceramic molecule bonding when the concentration of HAp was increased from 55% to 65% w/w. However, when the HAp concentration was increased to 75% and 85% w/w, the additional HAp particles did not bond with polymer molecules and directly attached on top of the filament surface to form small cracks. From this perspective, the *PCL/PEO/65%HAp* ink is the most suitable formulation for the DIW fabrication 3D scaffolds. The poor mechanical properties of PCL/PEO/85%HAp may be associated with the high porosity of this material (as indicated by micro CT analysis).

The elastic modulus and yield strength of PCL/PEO/HAp scaffolds fabricated in this study were in the range of 8.33 MPa to 12.33 MPa and 0.35 to 0.97 MPa, respectively, and were dependent on the HAp concentration. To the best of the authors' knowledge, the scaffold mechanical properties obtained in this study are higher than those reported in previous studies involving DIW printed PCL/HAp based scaffolds (22, 23). Previous studies indicate that the compressive elastic modulus of human cancellous bones is in the range of 1–900 MPa (1, 53-58). The pore size of cancellous bones varies between 50 and 850 µm; the porosity varies between 40 and 90% (59, 60). The horizontal and vertical filament distance/pore size, porosity, and elastic modulus of the PCL/PEO/HAp scaffold obtained in this study were similar to those of human cancellous bones. It should be noted that the scaffold porosity affects

the mechanical properties; for example, there is a linear relationship between scaffold porosity and elastic modulus (61). Apart from scaffold porosity, interconnectivity is also an important factor that would affect cell growth within the tissue scaffold. Ashworth, Mehr (62) developed percolation diameter theory to investigate scaffold interconnectivity in terms of a characteristic feature size for cell transport. The percolation diameter is the size of the largest spherical object able to travel through an infinitely large scaffold. Scaffolds with a certain percolation diameter will impede the transport of any object larger than this diameter. Since the micro-CT scan analysis results show the horizontal and vertical pore size/filament distance were larger than 0, the scaffolds developed in the study exhibited 100% interconnectivity. In comparison to traditional scaffold fabrication methods (e.g., freeze-drying or gas forming), 3D printing has the advantage of being able to prepare a scaffold with 100% interconnectivity. This attribute would be beneficial for vascularization and minimizing cell necrosis in the tissue scaffold (62-64).

The surface roughness had a substantial impact on scaffold surface wettability. The results showed that the rougher surfaces of the DIW printed scaffold were associated with lower contact angle values and better wettability; this result is in line with previous studies (65, 66). The relationship between roughness and wettability was noted by Wenzel (67), who indicated that surfaces with higher levels of roughness exhibit enhanced wettability.

The VAN drug was successfully loaded into the DIW printed PCL/PEO/HAp composite scaffolds. The VAN loaded PCL/PEO/HAp scaffolds exhibited a first-order immediate release mechanism and showed burst release within the first half-hour. The initial burst phenomenon was more prominent for *PCL/PEO/HAp_9%VAN* than for *PCL/PEO/HAp_3%VAN*. A similar trend was found in previous studies (25, 68, 69). This result may be attributed to the hydrophilic nature of VAN. The vancomycin molecules do not have a specific binding affinity to the components of the PCL/PEO/HAp scaffold. The VAN was distributed on the surface of filament before the release study as seen in the SEM image of Figure 11 (b); this initial burst release in the initial phase may be attributed to this morphology. Figure 11 (c) shows the surface morphology of the scaffold after release revealed that VAN was almost entirely eluted. Thus, the drug release results showed sudden drug release within a short period, particularly for the scaffold with a higher VAN concentration. Previous studies indicated that a tissue scaffold loaded with an antibiotic agent can relieve inflammation (26, 70, 71). If the scaffold with drug loading has a relatively rapid drug release rate, then it can be used for bone tissue application-related surgical hemostasis and anti-inflammatory conditions (72, 73). It is noted that apart from drug concentration and the interaction between the drug and the polymers, the scaffold geometry also has an influence on the drug release mechanism. Previous studies indicate (74, 75) that materials with higher porosity and surface/volume ratios exhibit a more rapid drug release profile; however, materials with higher porosity exhibit poor mechanical properties. Thus, the interrelation between scaffold geometry, drug release, and mechanical properties must be balanced based on each individual patient's requirements.

5 Conclusions

This study demonstrates the processing of biocomposite PCL/PEO/HAp inks with HAp concentrations from 55 to 85% w/w; woodpile scaffold structures with the formulated composite inks were successfully fabricated. The ink rheology properties, scaffold material properties, surface properties, and mechanical properties of the scaffold structures were investigated. The rheological data indicate that upon increasing the concentration of HAp, more marked shear-thinning behavior was observed. Based on the mathematical modeling analysis of ink conditions within the printing needle, the shear rate of the *PCL/PEO/85%HAp* ink was higher than that of other types of inks; while it had the lowest ink recover rate. Thus, the results suggest HAp concentration should be not higher than 75% w/w in PCL/PEO/HAp composite inks for scaffold fabrication using DIW printing. Compared with other types of scaffolds, the *PCL/PEO/65%HAp* scaffold had better wettability and higher mechanical properties. Furthermore, in vitro drug release demonstrated that the VAN-loaded scaffolds were capable of releasing VAN. The PCL/PEO/HAp composite developed in this study offers a new feedstock material for DIW printing of 3D scaffolds with antibacterial activity for bone tissue engineering applications.

Acknowledgments

The authors would like to acknowledge the USFDA Office of Science and Engineering Laboratories for use of the DHR-3 rheometer. The financial support of China Scholarship Council (CSC) - UCL Joint research scholarship, and the Vest Scholarship of the US National Academy of Engineering (NAE) are gratefully acknowledged.

Disclosure statement

There is no potential conflict of interest for this work.

Authorship contribution statement

Bin Zhang: design, experimentation, analysis, data curation, writing-original draft, writing-review & editing. Alexander K. Nguyen: experimentation, analysis, data curation, writing - review & editing. Roger Narayan: analysis, data curation, writing - review & editing, supervision. Jie Huang: analysis, data curation, writing - review & editing, supervision.

References:

1. Zhang B, Huang J, Narayan R. Gradient scaffolds for osteochondral tissue engineering and regeneration. Journal of Materials Chemistry B. 2020.
2. Williams GM, Chan EF, Temple-Wong MM, Bae WC, Masuda K, Bugbee WD, et al. Shape, loading, and motion in the bioengineering design, fabrication, and testing of personalized synovial joints. Journal of biomechanics. 2010;43(1):156-65.
3. Minas T. Autologous chondrocyte implantation for focal chondral defects of the knee. Clinical Orthopaedics and Related Research®. 2001;391:S349-S61.
4. Bauer TW, Muschler GF. Bone graft materials: an overview of the basic science. Clinical Orthopaedics and Related Research®. 2000;371:10-27.
5. Miron RJ SA, Shuang Y, Bosshardt DD, Gruber R, Buser D, Chandad F, Zhang Y. Osteoinductive potential of a novel biphasic calcium phosphate bone graft in comparison with autographs, xenografts, and DFDBA. Clinical Oral Implants. 2015.
6. Loh QL, Choong C. Three-dimensional scaffolds for tissue engineering applications: role of porosity and pore size. Tissue Engineering Part B: Reviews. 2013;19(6):485-502.
7. Reichert JC, Wullschleger ME, Cipitria A, Lienau J, Cheng TK, Schütz MA, et al. Custom-made composite scaffolds for segmental defect repair in long bones. International orthopaedics. 2011;35(8):1229-36.
8. Hutmacher D, Cool S. Concepts of scaffold-based tissue engineering—the rationale to use solid free-form fabrication techniques. Journal of cellular and molecular medicine. 2007;11(4):654-69.
9. Farto-Vaamonde X, Auriemma G, Aquino RP, Concheiro A, Alvarez-Lorenzo C. Post-manufacture loading of filaments and 3D printed PLA scaffolds with prednisolone and dexamethasone for tissue regeneration applications. European Journal of Pharmaceutics and Biopharmaceutics. 2019;141:100-10.
10. Jang J, Park JY, Gao G, Cho DW. Biomaterials-based 3D cell printing for next-generation therapeutics and diagnostics. Biomaterials. 2018;156:88-106.
11. Lewis JA, Gratson GM. Direct writing in three dimensions. Materials Today. 2004;7(7):32-9.
12. Dávila JL, d'Ávila MA. Rheological evaluation of Laponite/alginate inks for 3D extrusion-based printing. The International Journal of Advanced Manufacturing Technology. 2019;101(1-4):675-86.
13. Barry III RA, Shepherd RF, Hanson JN, Nuzzo RG, Wiltzius P, Lewis JA. Direct-Write Assembly of 3D Hydrogel Scaffolds for Guided Cell Growth. Advanced Materials. 2009;21(23):2407-10.
14. Zhang B, Cristescu R, Chrisey D, Narayan R. Solvent-based Extrusion 3D Printing for the Fabrication of Tissue Engineering Scaffolds. International Journal of Bioprinting. 2020;6:19.
15. Paxton N, Smolan W, Böck T, Melchels F, Groll J, Jungst T. Proposal to assess printability of bioinks for extrusion-based bioprinting and evaluation of rheological properties governing bioprintability. Biofabrication. 2017;9(4):044107.
16. Song R, Murphy M, Li C, Ting K, Soo C, Zheng Z. Current development of biodegradable polymeric materials for biomedical applications. Drug design, development and therapy. 2018;12:3117.
17. Jiao Z, Luo B, Xiang S, Ma H, Yu Y, Yang W. 3D printing of HA/PCL composite tissue engineering scaffolds. Advanced Industrial and Engineering Polymer Research. 2019;2(4):196-202.
18. Remya K, Chandran S, Mani S, John A, Ramesh P. Hybrid Polycaprolactone/Polyethylene oxide scaffolds with tunable fiber surface morphology, improved hydrophilicity and biodegradability for bone tissue engineering applications. Journal of Biomaterials Science, Polymer Edition. 2018;29(12):1444-62.
19. Turner-Walker GH. The characterisation of fossil bone: Durham University; 1993.
20. Bruyas A, Lou F, Stahl AM, Gardner M, Maloney W, Goodman S, et al. Systematic characterization of 3D-printed PCL/β-TCP scaffolds for biomedical devices and bone tissue engineering: Influence of composition and porosity. Journal of materials research. 2018;33(14):1948.
21. Ma PX, Zhang R, Xiao G, Franceschi R. Engineering new bone tissue in vitro on highly porous poly (α-hydroxyl acids)/hydroxyapatite composite scaffolds. Journal of Biomedical Materials Research: An Official Journal of The Society for Biomaterials and The Japanese Society for Biomaterials. 2001;54(2):284-93.
22. Cui Z, Nelson B, Peng Y, Li K, Pilla S, Li W-J, et al. Fabrication and characterization of injection molded poly (ε-caprolactone) and poly (ε-caprolactone)/hydroxyapatite scaffolds for tissue engineering. Materials Science and Engineering: C. 2012;32(6):1674-81.
23. Kim J-W, Shin K-H, Koh Y-H, Hah MJ, Moon J, Kim H-E. Production of poly (ε-caprolactone)/hydroxyapatite composite scaffolds with a tailored macro/micro-porous structure, high mechanical properties, and excellent bioactivity. Materials. 2017;10(10):1123.
24. Bailie GR, Neal D. Vancomycin ototoxicity and nephrotoxicity. Medical toxicology and adverse drug experience. 1988;3(5):376-86.
25. Weng W, Nie W, Zhou Q, Zhou X, Cao L, Ji F, et al. Controlled release of vancomycin from 3D porous graphene-based composites for dual-purpose treatment of infected bone defects. RSC Advances. 2017;7(5):2753-65.
26. Rai A, Senapati S, Saraf SK, Maiti P. Biodegradable poly (ε-caprolactone) as a controlled drug delivery vehicle of vancomycin for the treatment of MRSA infection. Journal of Materials Chemistry B. 2016;4(30):5151-60.

27. Ghaffar I, Imran M, Perveen S, Kanwal T, Saifullah S, Bertino MF, et al. Synthesis of chitosan coated metal organic frameworks (MOFs) for increasing vancomycin bactericidal potentials against resistant S. aureus strain. Materials Science and Engineering: C. 2019;105:110111.
28. Zhang B, Chung SH, Barker S, Craig D, Narayan RJ, Huang J. Direct ink writing of polycaprolactone / polyethylene oxide based 3D constructs. Progress in Natural Science: Materials International. 2020.
29. Morrison F. Understanding Rheology Oxford University Press. New York. 2001.
30. Macosko CW, Larson RG. Rheology: principles, measurements, and applications. 1994.
31. Goncalves EM, Oliveira FJ, Silva RF, Neto MA, Fernandes MH, Amaral M, et al. Three-dimensional printed PCL-hydroxyapatite scaffolds filled with CNT s for bone cell growth stimulation. Journal of Biomedical Materials Research Part B: Applied Biomaterials. 2016;104(6):1210-9.
32. Dorj B, Won JE, Kim JH, Choi SJ, Shin US, Kim HW. Robocasting nanocomposite scaffolds of poly (caprolactone)/hydroxyapatite incorporating modified carbon nanotubes for hard tissue reconstruction. Journal of Biomedical Materials Research Part A. 2013;101(6):1670-81.
33. Blair GS, Hening J, Wagstaff A. The Flow of Cream through Narrow Glass Tubes. Journal of physical chemistry. 1939;43(7):853-64.
34. Peak CW, Stein J, Gold KA, Gaharwar AK. Nanoengineered colloidal inks for 3D bioprinting. Langmuir. 2018;34(3):917-25.
35. Roopavath UK, Malferrari S, Van Haver A, Verstreken F, Rath SN, Kalaskar DM. Optimization of extrusion based ceramic 3D printing process for complex bony designs. Materials & Design. 2019;162:263-70.
36. Hao L, Tang D, Sun T, Xiong W, Feng Z, Evans KE, et al. Direct Ink Writing of Mineral Materials: A review. International Journal of Precision Engineering and Manufacturing-Green Technology. 2020:1-21.
37. Zocca A, Colombo P, Gomes CM, Günster J. Additive manufacturing of ceramics: issues, potentialities, and opportunities. Journal of the American Ceramic Society. 2015;98(7):1983-2001.
38. Chen Z, Li Z, Li J, Liu C, Liu C, Li Y, et al. 3D printing of ceramics: a review. Journal of the European Ceramic Society. 2018.
39. Diaz-Gomez L, Kontoyiannis PD, Melchiorri AJ, Mikos AG. Three-dimensional printing of tissue engineering scaffolds with horizontal pore and composition gradients. Tissue Engineering Part C: Methods. 2019;25(7):411-20.
40. Grebenyuk S, Ranga A. Engineering organoid vascularization. Frontiers in bioengineering and biotechnology. 2019;7:39.
41. Kunzler TP, Drobek T, Schuler M, Spencer ND. Systematic study of osteoblast and fibroblast response to roughness by means of surface-morphology gradients. Biomaterials. 2007;28(13):2175-82.
42. Dubey P, Bhushan B, Sachdev A, Matai I, Uday Kumar S, Gopinath P. Silver-nanoparticle-incorporated composite nanofibers for potential wound-dressing applications. Journal of Applied Polymer Science. 2015;132(35).
43. Abdelrazek E, Hezma A, El-Khodary A, Elzayat A. Spectroscopic studies and thermal properties of PCL/PMMA biopolymer blend. Egyptian Journal of Basic and Applied Sciences. 2016;3(1):10-5.
44. Nasir NM, Zain NM, Raha M, Kadri N. Characterization of chitosan-poly (ethylene oxide) blends as haemodialysis membrane. American Journal of Applied Sciences. 2005;2(12):1578-83.
45. Ragu A, Senthilarasan K, Sakthivel P. Synthesis and characterization of nano hydroxyapatite with poly vinyl pyrrolidone nano composite for bone tissue regeneration. Int J Eng Res Appl. 2014;4(10):50-4.
46. Zarif M, Afidah A, Abdullah J, Shariza A. Physicochemical characterization of vancomycin and its complexes with?-cyclodextrin. 2012.
47. Potrč T, Baumgartner S, Roškar R, Planinšek O, Lavrič Z, Kristl J, et al. Electrospun polycaprolactone nanofibers as a potential oromucosal delivery system for poorly water-soluble drugs. European Journal of Pharmaceutical Sciences. 2015;75:101-13.
48. Rychter M, Baranowska-Korczyc A, Milanowski B, Jarek M, Maciejewska BM, Coy EL, et al. Cilostazol-loaded poly (ε-Caprolactone) electrospun drug delivery system for cardiovascular applications. Pharmaceutical research. 2018;35(2):32.
49. Zhang B, Cristescu R, Chrisey DB, Narayan RJ. Solvent-based Extrusion 3D Printing for the Fabrication of Tissue Engineering Scaffolds. International Journal of Bioprinting. 2020;6(1).
50. Chen DX, Chen, Glaser. Extrusion bioprinting of scaffolds for tissue engineering applications: Springer; 2019.
51. Kumar A, Kargozar S, Baino F, Han SS. Additive manufacturing methods for producing hydroxyapatite and hydroxyapatite-based composite scaffolds: A review. Front Mater 6: 313 doi: 103389/fmats. 2019.
52. Liu J, Li L, Suo H, Yan M, Yin J, Fu J. 3D printing of biomimetic multi-layered GelMA/nHA scaffold for osteochondral defect repair. Materials & Design. 2019;171:107708.
53. Athanasiou K, Agarwal A, Dzida F. Comparative study of the intrinsic mechanical properties of the human acetabular and femoral head cartilage. Journal of Orthopaedic Research. 1994;12(3):340-9.
54. Boschetti F, Pennati G, Gervaso F, Peretti GM, Dubini G. Biomechanical properties of human articular cartilage under compressive loads. Biorheology. 2004;41(3-4):159-66.
55. Gibson LJ. The mechanical behaviour of cancellous bone. Journal of biomechanics. 1985;18(5):317-28.
56. Sabree I, Gough J, Derby B. Mechanical properties of porous ceramic scaffolds: influence of internal dimensions. Ceramics International. 2015;41(7):8425-32.
57. Antons J, Marascio MGM, Nohava J, Martin R, Applegate L, Bourban P, et al. Zone-dependent mechanical properties of human articular cartilage obtained by indentation measurements. Journal of Materials Science: Materials in Medicine. 2018;29(5):57.
58. Oladapo BI, Zahedi S, Adeoye A. 3D printing of bone scaffolds with hybrid biomaterials. Composites Part B: Engineering. 2019;158:428-36.

59. Morgan EF, Unnikrisnan GU, Hussein AI. Bone mechanical properties in healthy and diseased states. Annual review of biomedical engineering. 2018;20:119-43.
60. Doktor T, Valach J, Kytýr D, Jiroušek O. Pore size distribution of human trabecular bone: Comparison of intrusion measurements with image analysis. Engineering Mechanics. 2011;115:2011.
61. Zhang B, Guo L, Chen H, Ventikos Y, Narayan RJ, Huang J. Finite element evaluations of the mechanical properties of polycaprolactone/hydroxyapatite scaffolds by direct ink writing: Effects of pore geometry. Journal of the Mechanical Behavior of Biomedical Materials. 2020:103665.
62. Ashworth JC, Mehr M, Buxton PG, Best SM, Cameron RE. Cell invasion in collagen scaffold architectures characterized by percolation theory. Advanced healthcare materials. 2015;4(9):1317-21.
63. Askari M, Naniz MA, Kouhi M, Saberi A, Zolfagharian A, Bodaghi M. Recent progress in extrusion 3D bioprinting of hydrogel biomaterials for tissue regeneration: a comprehensive review with focus on advanced fabrication techniques. Biomaterials science. 2021;9(3):535-73.
64. Kačarević ŽP, Rider PM, Alkildani S, Retnasingh S, Smeets R, Jung O, et al. An introduction to 3D bioprinting: possibilities, challenges and future aspects. Materials. 2018;11(11):2199.
65. AlRatrout A, Blunt MJ, Bijeljic B. Wettability in complex porous materials, the mixed-wet state, and its relationship to surface roughness. Proceedings of the National Academy of Sciences. 2018;115(36):8901-6.
66. Yorur H, Erer A, Oğuz S, editors. Effect of surface roughness on wettability of adhesive on wood substrates. 3rd International Conference on Science, Ecology and Technology; 2017.
67. Wenzel RN. Resistance of solid surfaces to wetting by water. Industrial & Engineering Chemistry. 1936;28(8):988-94.
68. Kim H-W, Knowles JC, Kim H-E. Hydroxyapatite porous scaffold engineered with biological polymer hybrid coating for antibiotic Vancomycin release. Journal of materials science: materials in medicine. 2005;16(3):189-95.
69. Parker T, Davé V, Falotico R, Zhao J, Nguyen T, He S, et al. Control of cilostazol release kinetics and direction from a stent using a reservoir-based design. Journal of Biomedical Materials Research Part B: Applied Biomaterials. 2012;100(3):603-10.
70. Roseti L, Parisi V, Petretta M, Cavallo C, Desando G, Bartolotti I, et al. Scaffolds for bone tissue engineering: state of the art and new perspectives. Materials Science and Engineering: C. 2017;78:1246-62.
71. Sahranavard M, Zamanian A, Ghorbani F, Shahrezaee MH. A critical review on three dimensional-printed chitosan hydrogels for development of tissue engineering. Bioprinting. 2020;17:e00063.
72. Mahanta AK, Patel DK, Maiti P. Nanohybrid scaffold of chitosan and functionalized graphene oxide for controlled drug delivery and bone regeneration. ACS Biomaterials Science & Engineering. 2019;5(10):5139-49.
73. Porter JR, Ruckh TT, Popat KC. Bone tissue engineering: a review in bone biomimetics and drug delivery strategies. Biotechnology progress. 2009;25(6):1539-60.
74. Zhang B, Nasereddin J, McDonagh T, von Zeppelin D, Gleadall A, Alqahtani F, et al. Effects of porosity on drug release kinetics of swellable and erodible porous pharmaceutical solid dosage forms fabricated by hot melt droplet deposition 3D printing. International Journal of Pharmaceutics. 2021:120626.
75. Sadia M, Arafat B, Ahmed W, Forbes RT, Alhnan MA. Channelled tablets: An innovative approach to accelerating drug release from 3D printed tablets. Journal of Controlled Release. 2018;269:355-63.

Table 1. The material composition of samples with and without VAN loading[a].

Scaffold names	PCL conc. (w/w)	PEO conc. (w/w)	HAp conc. (w/w)	HAp conc. (v/v)	VAN conc. (w/w)
PCL/PEO/55%HAp	22.5%	22.5%	55%	30.2%	0
PCL/PEO/65%HAp	17.5%	17.5%	65%	39.5%	0
PCL/PEO/75%HAp	12.5%	12.5%	75%	51.3%	0
PCL/PEO/85%HAp	7.5%	7.5%	85%	66.3%	0
PCL/PEO/HAp_3%VAN	17%	17%	63%	38.4%	3%
PCL/PEO/HAp_3%VAN	15.5%	15.5%	60%	36.2%	9%

[a]The percentage of polymers, HAp and VAN is related to dry solute.

Table 2. The comparison of designed theoretical values of CAD structures and DIW printed 3D scaffolds. Values represent means and standard error of N=3; the width, length, and thickness of DIW printed *PCL/PEO/85%HAp* scaffold was significant higher ($P \leq 0.05$) than *PCL/PEO/55%HAp*.

	Width (mm)	Length (mm)	Thickness (mm)
Theoretical value	14	14	5
Experimental value			
PCL/PEO/55%HAp	12.65 ± 0.23	12.50 ± 0.20	4.24 ± 0.03
PCL/PEO/65%HAp	12.89 ± 0.24	12.95 ± 0.16	4.43 ± 0.08
PCL/PEO/75%HAp	13.53 ± 0.10	13.55 ± 0.26	4.64 ± 0.09
PCL/PEO/85%HAp	13.95 ± 0.03	13.83 ± 0.10	4.67 ± 0.06

Table 3. Roughness parameters (Ra, Rz, Rq) for the DIW printed samples - *PCL/PEO/55%HAp*, *PCL/PEO/65%HAp*, *PCL/PEO/75%HAp*, and *PCL/PEO/85%HAp*. Values represent means and standard error of N=3. The surface roughness of *PCL/PEO/65%HAp* was significantly higher ($p \leq 0.05$) than that of *PCL/PEO/55%HAp*.

Sample name	Roughness parameters (μm)		
	Ra	Rz	Rq
PCL/PEO/55%HAp	1.95 ± 0.09	10.82 ± 0.44	2.34 ± 0.10
PCL/PEO/65%HAp	2.98 ± 0.14	17.49 ± 1.09	3.70 ± 0.20
PCL/PEO/75%HAp	2.57 ± 0.25	16.18 ± 1.30	3.25 ± 0.34
PCL/PEO/85%HAp	2.91 ± 0.14	16.42 ± 0.46	3.58 ± 0.17

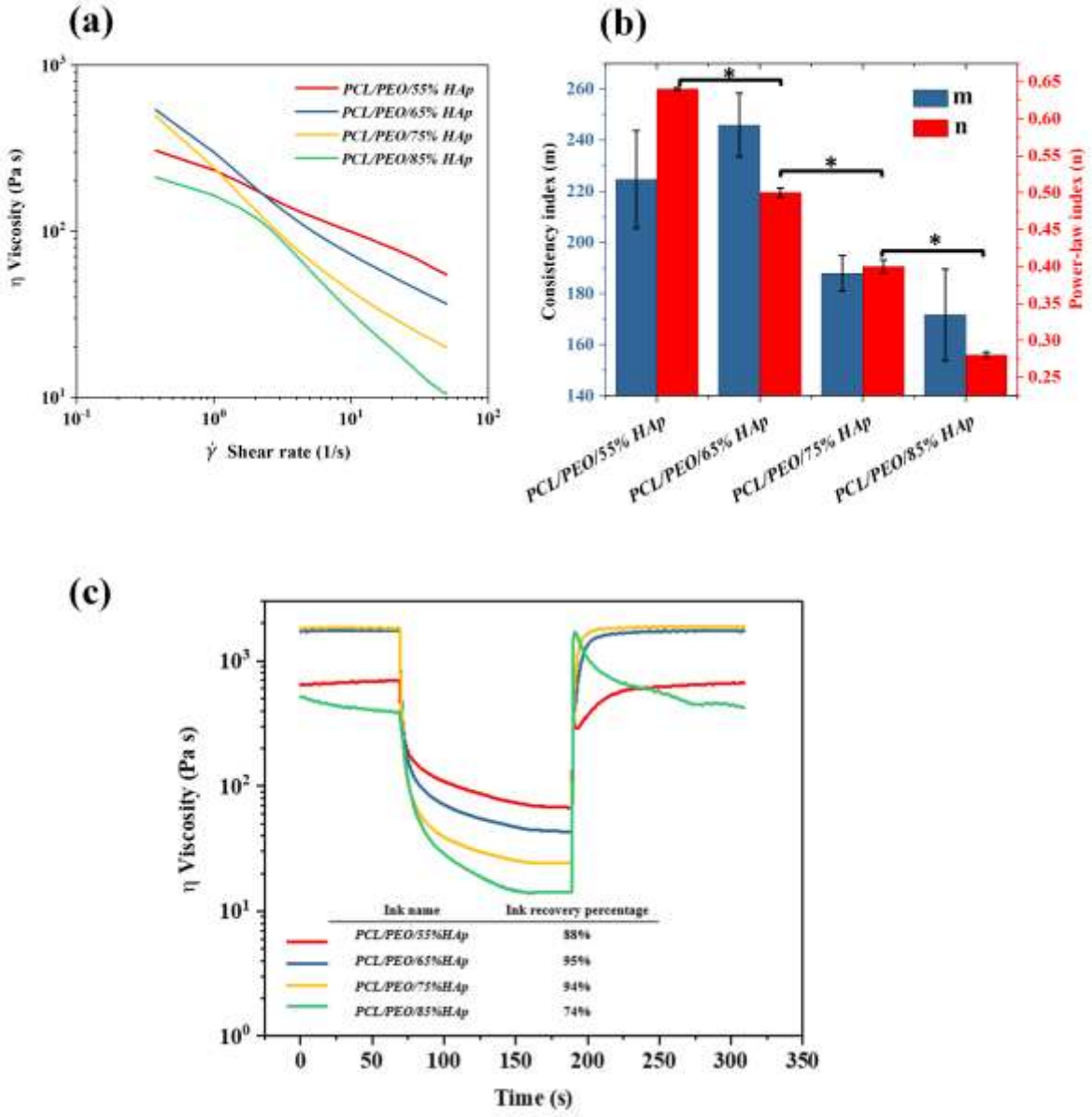

Figure 1. (a) The shear rate-viscosity flow curves. (b) Power law model fitting parameters, consistency index (*m*) and power-law index (*n*), for the *PCL/PEO/55%HAp*, *PCL/PEO/65%HAp*, *PCL/PEO/75%HAp*, and *PCL/PEO/85%HAp* inks. Values represent means and standard error of N=5, asterisk (*) represents $p \leq 0.05$. (c) Viscosity as a function of the time for the creep recovery test among PCL/PEO/HAp inks. The inserted table includes the viscosity recovery percentages that were calculated from the creep recovery test.

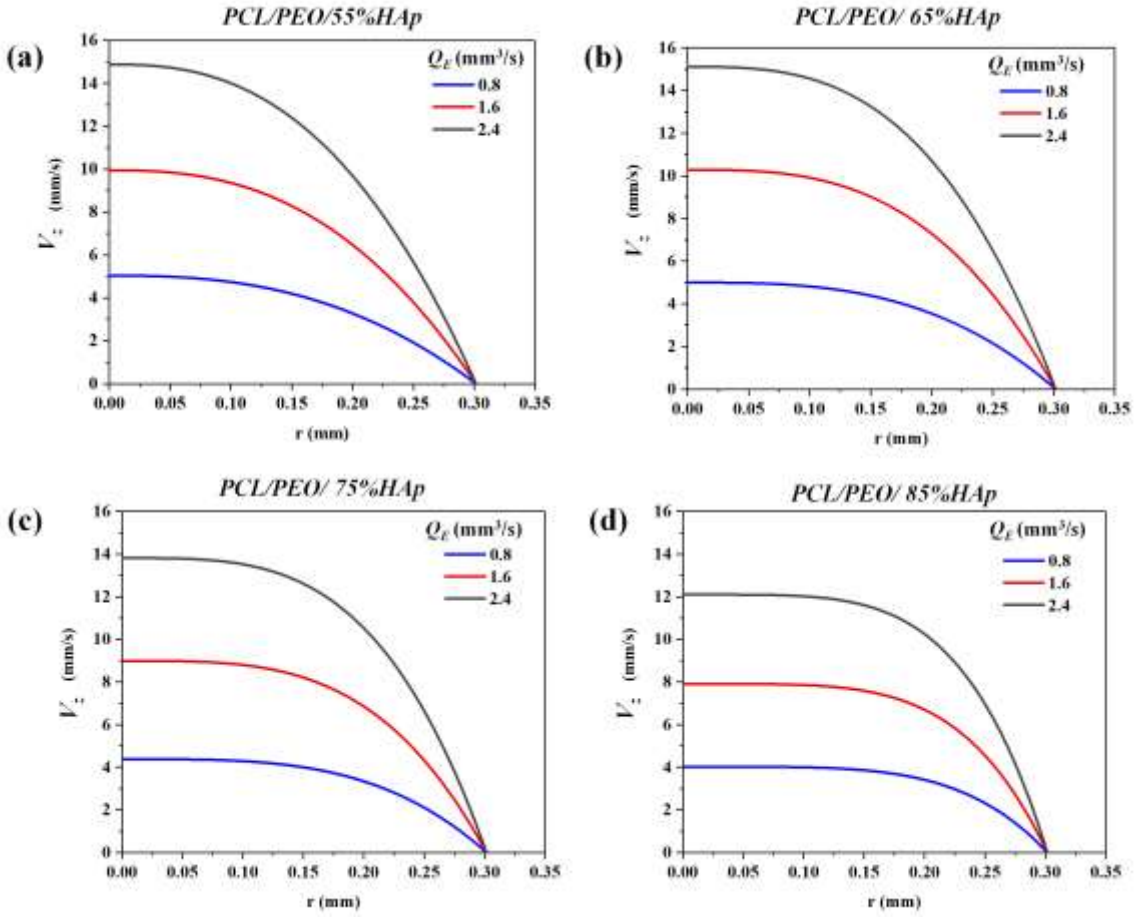

Figure 2. The ink velocity (Z direction) (V_Z) profile inside a printing nozzle for inks of *PCL/PEO/55%HAp* (a), *PCL/PEO/65%HAp* (b), *PCL/PEO/75%HAp* (c) and *PCL/PEO/85%HAp* (d).

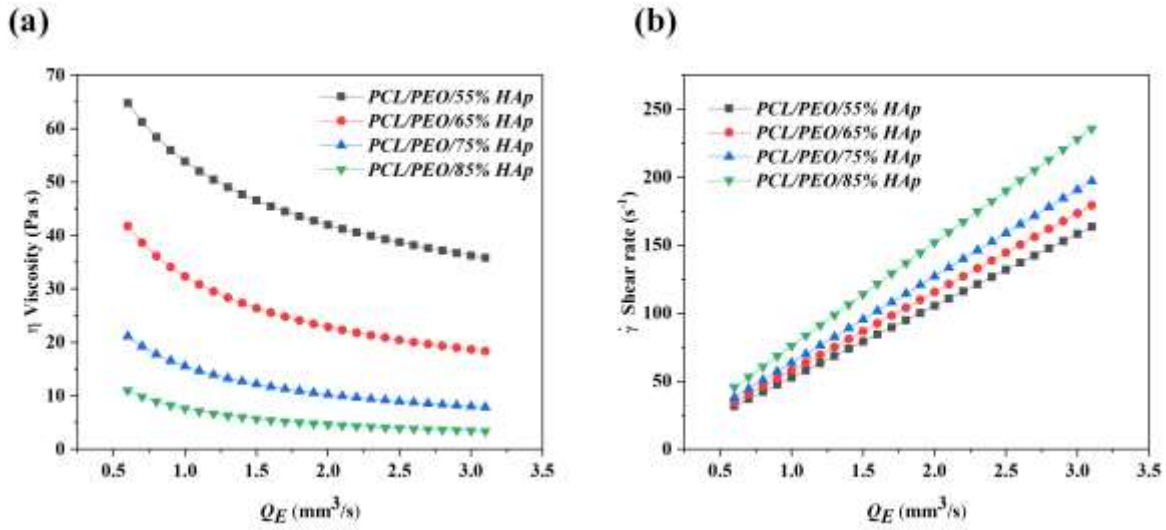

Figure 3. The DIW printing viscosity (a) and wall shear rate (b) as a function of the extrusion fluid rate for the *PCL/PEO/55%HAp*, *PCL/PEO/65%HAp*, *PCL/PEO/75%Hap*, and *PCL/PEO/85%HAp* inks.

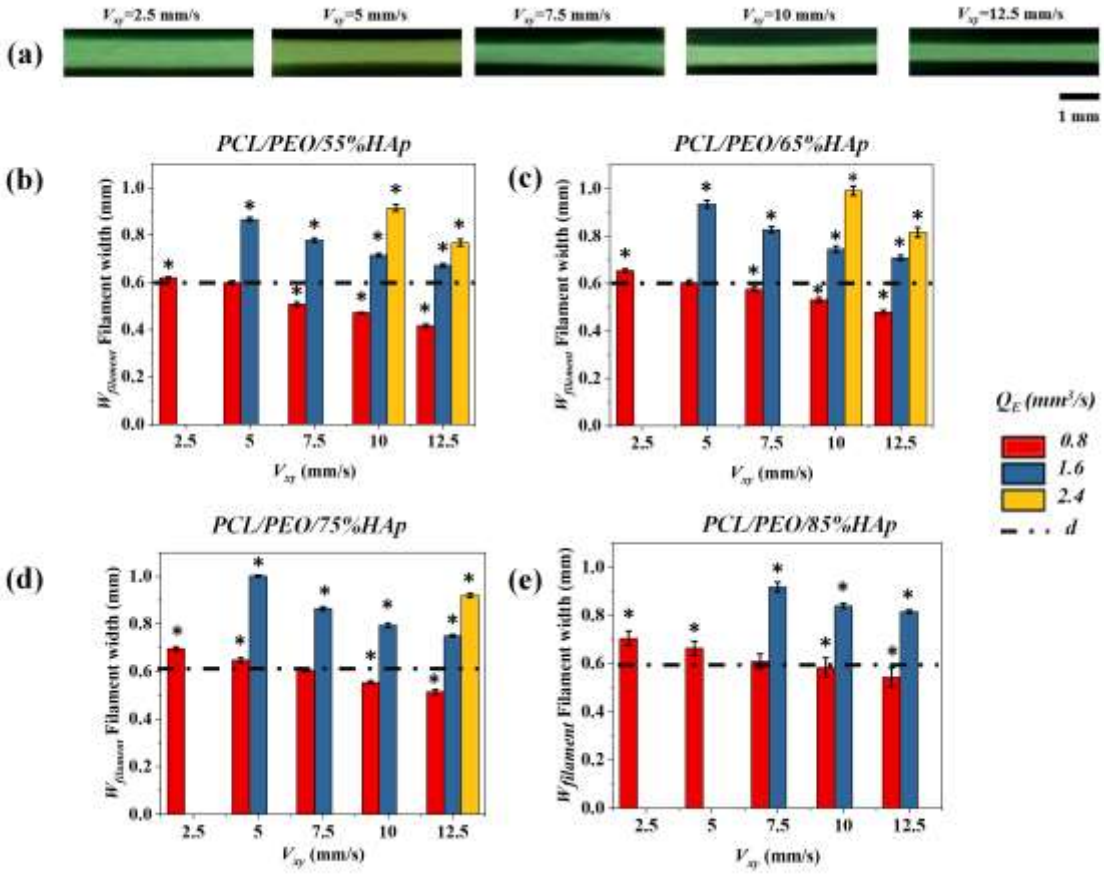

Figure 4. (a) The printed filament width of ink *PCL/PEO/55%HAp* decreases with the increased print speed (V_{XY}) when the extrusion rate (Q_E) as 0.8 mm^3/s, the scale bar is 1 mm; the DIW printed filament width compared with the applied nozzle diameter (d = 603 μm) at the designated printing speed (V_{XY}) and extrusion rate (Q_E) with *PCL/PEO/55%HAp* (b), *PCL/PEO/65%HAp* (c), *PCL/PEO/75%HAp* (d), and *PCL/PEO/85%HAp* (e) inks. Values represent means and standard error of N=50 (measurement on multiple measurements on multiple filaments). Asterisk (*) represents p≤0.05, which indicates that there was a significant difference from the ideal value (d=603 μm).

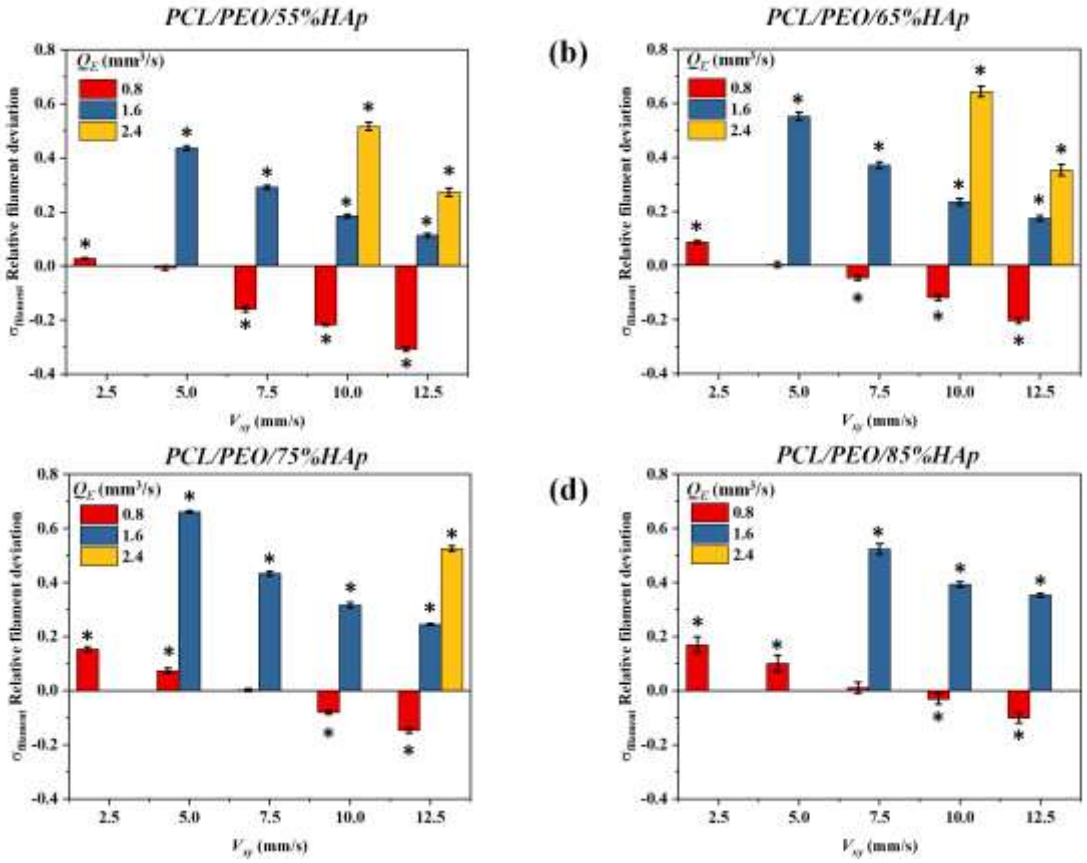

Figure 5. Relative filament deviation ($\sigma_{filament}$) as an index to evaluate the DIW printed filament width under the designated printing speed (V_{XY}) and extrusion rate (Q_E) with *PCL/PEO/55%HAp* (a), *PCL/PEO/65%HAp* (b), *PCL/PEO/75%HAp* (c), and *PCL/PEO/85%HAp* (d) inks. Values represent means and standard error of N=50 (measurement on multiple measurements on multiple filaments). Asterisk (*) represents p≤0.05, which indicates that there was a significant difference from the ideal value (d=603 μm).

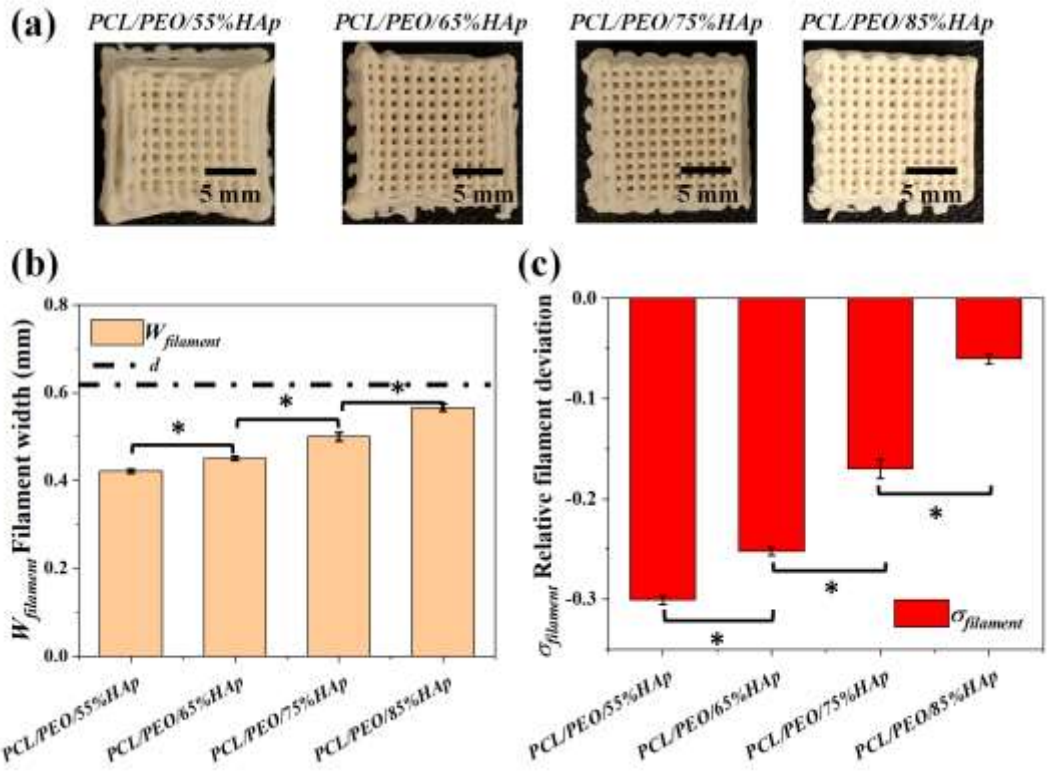

Figure 6. Scaffold image (a) and the measured filament width ($W_{filament}$) compared with the applied nozzle diameter (d = 603 µm) (b) and the relative filament deviation ($\sigma_{filament}$) (c) of the DIW printed 3D scaffolds. Values represent means and standard error of N=50. (measurement on multiple measurements on multiple filaments). Asterisk (*) represents p≤0.05; there was a significant difference in filament width and the relative filament deviation among *PCL/PEO/55%HAp*, *PCL/PEO/65%HAp*, *PCL/PEO/75%HAp*, and *PCL/PEO/85%HAp*.

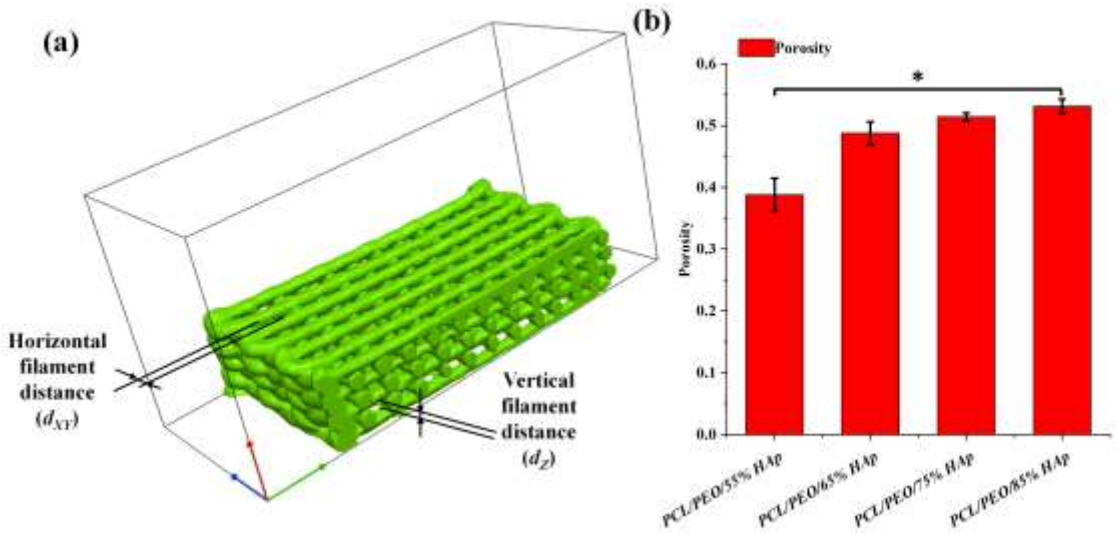

Figure 7. (a) Micro-CT scan generated 3D model of DIW printed PCL/PEO/HAp scaffold (example of *PCL/PEO/85%HAp*). (b) Porosity of the DIW printed PCL/PEO/HAp 3D construct. Values represent means and standard error of N=3. Asterisk (*) represents $p \leq 0.05$.

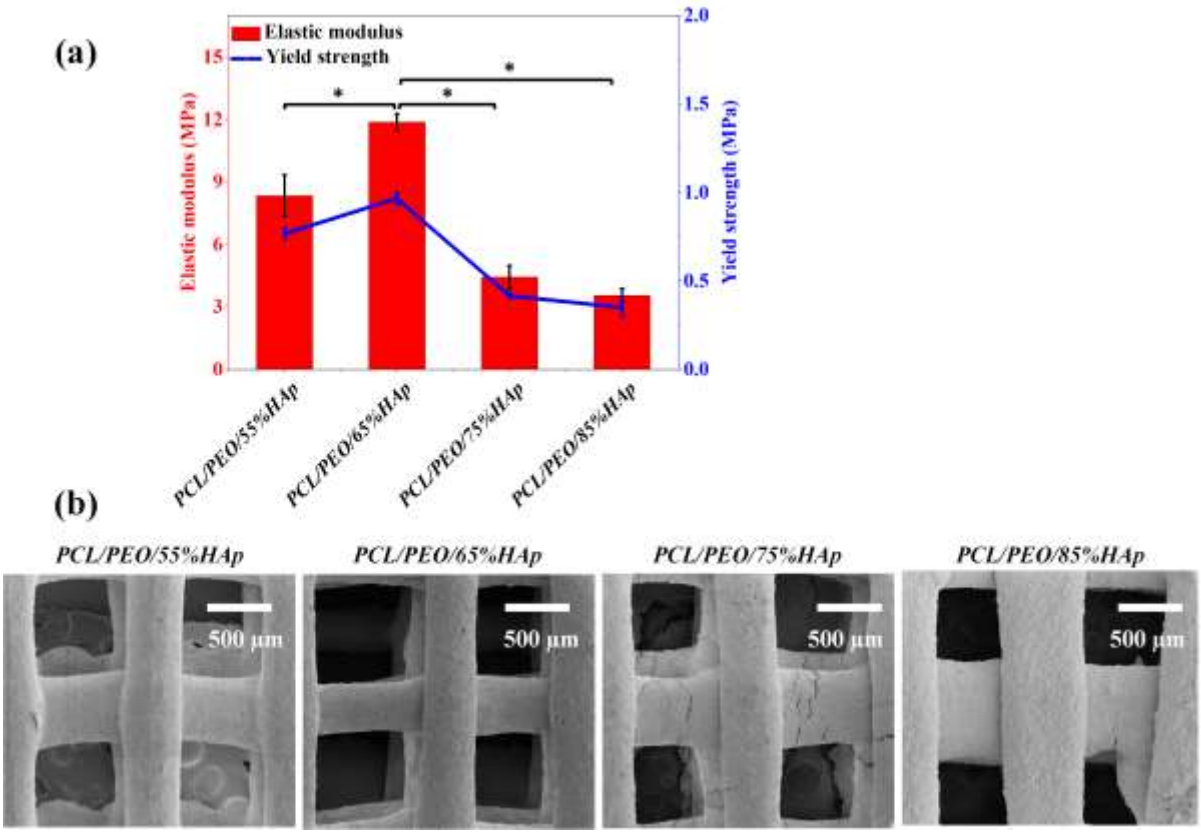

Figure 8. (a) The elastic modulus and yield strength of DIW printed scaffolds; the images shown in the inserts are the DIW printed PCL/PEO/HAp scaffolds *PCL/PEO/55%HAp*, *PCL/PEO/65%HAp*, *PCL/PEO/75%HAp*, and *PCL/PEO/85%HAp* (scale bar=5 mm). Values represent mean and standard error values of N=4. Asterisk (*) represents $p \leq 0.05$. (c) SEM images collected on the pristine DIW printed samples (i.e., before mechanical testing).

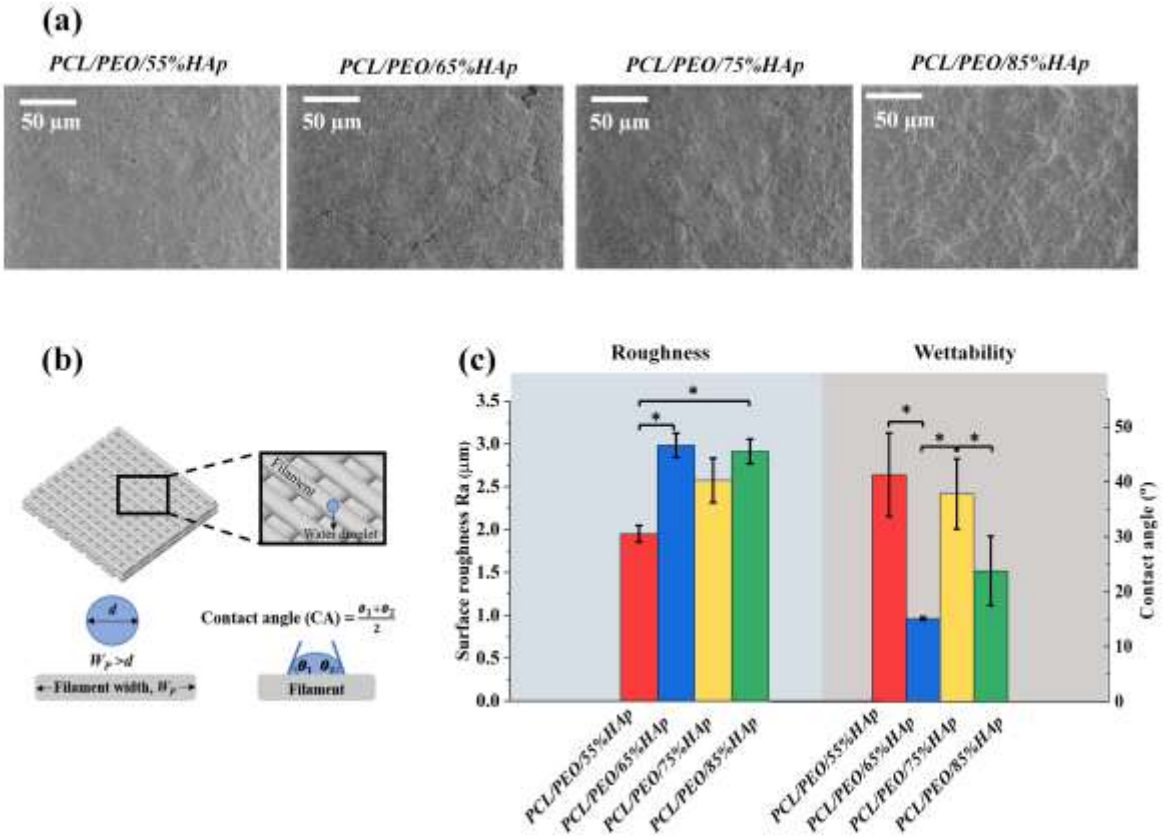

Figure 9. (a) SEM images showing the surface morphology of the DIW printed scaffolds. (b) Schematic diagram of contact angle values. (c) The roughness and initial CA results (drop age = 0 second) on the filament surface of the DIW printed samples - *PCL/PEO/55%HAp, PCL/PEO/65%HAp, PCL/PEO/75%HAp*, and *PCL/PEO/85%HAp*. Values represent means and standard error of N=3. Asterisk (*) represents $p \leq 0.05$.

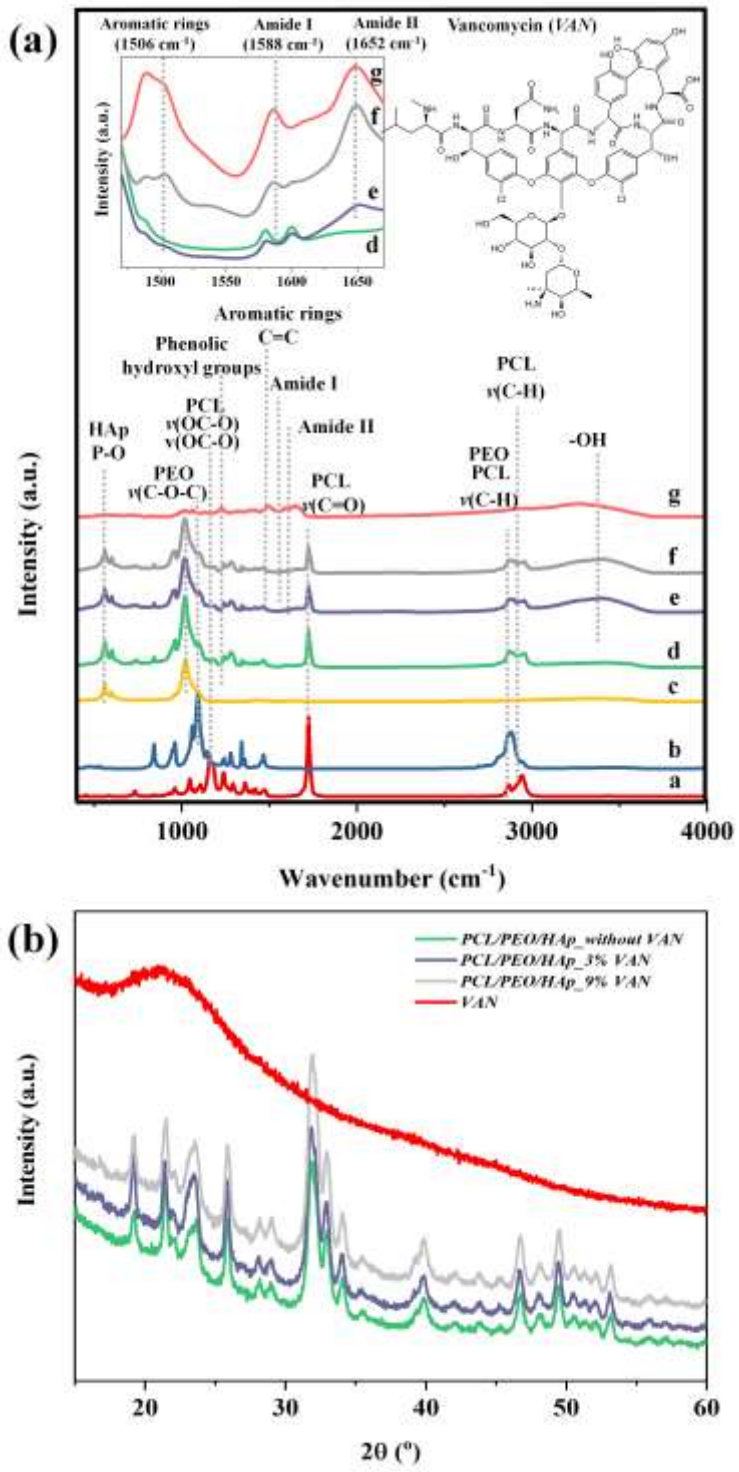

Figure 10. (a) FTIR spectra of PCL (a), PEO (b), HAp (c), DIW printed *PCL/PEO/65%HAp* scaffold (d), *PCL/PEO/HAp_3%VAN* scaffold (e), *PCL/PEO/HAp_9%VAN* scaffold (f) and VAN (g). The insert shows the stacked spectra of VAN and PCL/PEO/HAp scaffolds with and without VAN; the intensity of the VAN peak at 1662 cm^{-1} increases with increasing VAN content. (b) PXRD patterns of the DIW printed PCL/PEO/65%HA scaffold (i.e., PCL/PEO/HAp without VAN), *PCL/PEO/HAp_3%VAN* scaffold, *PCL/PEO/HAp_9%VAN* scaffold, and VAN powder; the VAN amount does not affect the crystallinity of the DIW printed PCL/PEO/HAp scaffold.

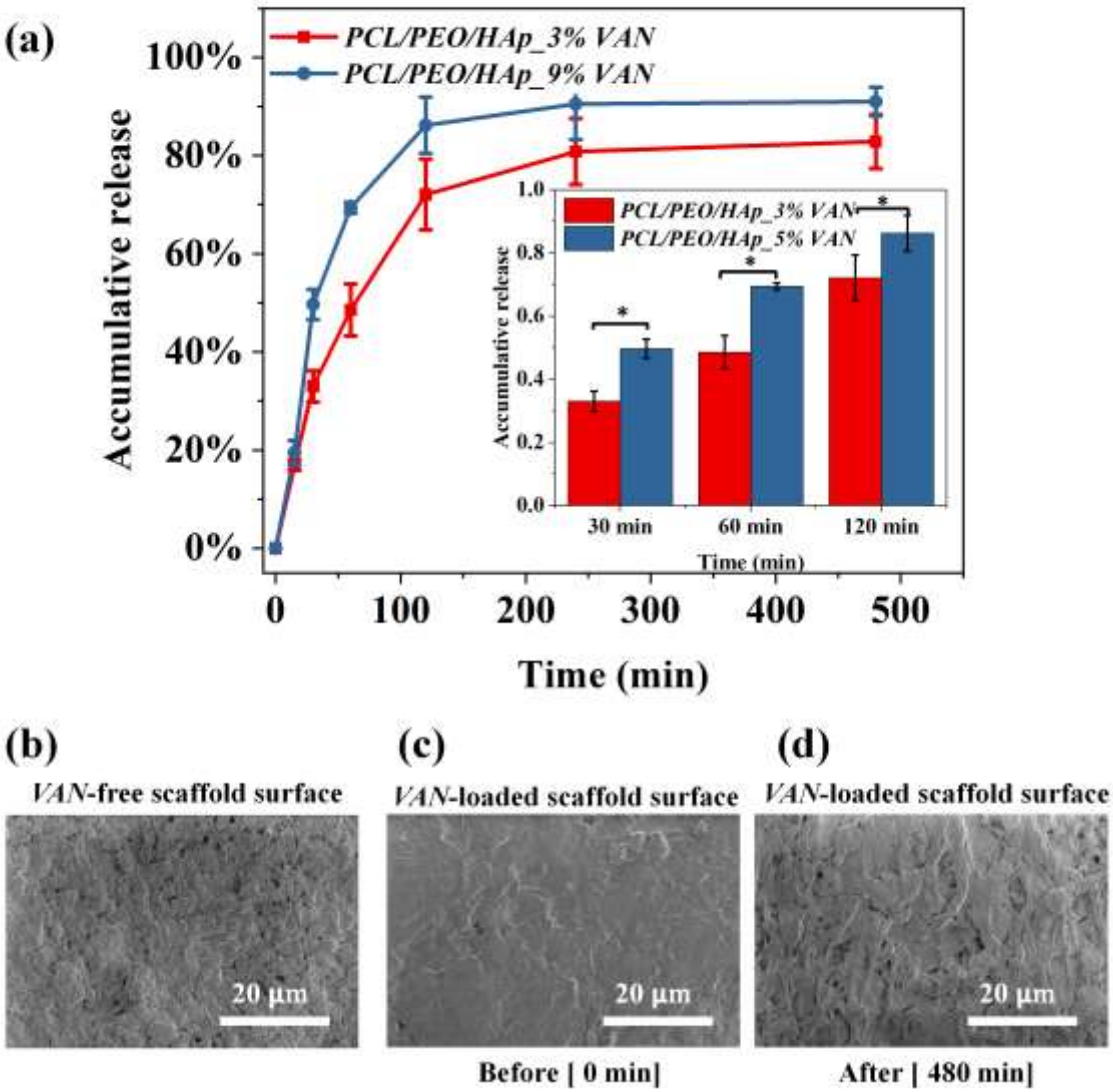

Figure 11. (a) VAN release profiles from the DIW printed samples *PCL/PEO/HAp_3%VAN* and *PCL/PEO/HAp_9%VAN* in PBS (pH=7.4) at a temperature of 37ºC. Values represent means and standard error of N=3. Asterisk (*) represents $p \leq 0.05$. (b) SEM images of the VAN-free scaffold surface. VAN-loaded scaffold surface before (c) and after (d) *PCL/PEO/HAp_9%VAN* release studies.